symmetry

MDPI

Article

IDM Benchmarks for the LHC and Future Colliders

Jan Kalinowski [1], Tania Robens [2,*], Dorota Sokołowska [1,3] and Aleksander Filip Żarnecki [1]

[1] Faculty of Physics, University of Warsaw, ul. Pasteura 5, 02–093 Warsaw, Poland; Jan.Kalinowski@fuw.edu.pl (J.K.); dorota.aniela.sokolowska@gmail.com (D.S.); Filip.Zarnecki@fuw.edu.pl (A.F.Ż.)
[2] Theoretical Physics Division, Rudjer Boskovic Institute, 10002 Zagreb, Croatia
[3] International Institute of Physics, Universidade Federal do Rio Grande do Norte, Campus Universitario, Lagoa Nova, Natal 59078-970, RN, Brazil
* Correspondence: trobens@irb.hr

Abstract: We present cross-section expectations for various processes and collider options, for benchmark scenarios of the Inert Doublet Model, a Two Higgs Doublet Model with a dark matter candidate. The proposed scenarios are consistent with current dark matter constraints, including the most recent bounds from the XENON1T experiment and relic density, as well as with known collider and low-energy limits. These benchmarks, chosen in earlier work for studies at e^+e^- colliders, exhibit a variety of kinematic features that should be explored at current and future runs of the LHC. We provide cross sections for all relevant production processes at 13 TeV, 27 TeV and 100 TeV proton collider, as well as for a possible 10 TeV and 30 TeV muon collider.

Keywords: collider phenomenology; beyond the Standard Model Physics; extended scalar sectors; future colliders; dark matter

Citation: Kalinowski, J.; Robens, T.; Sokołowska, D.; Żarnecki, A.F. IDM Benchmarks for the LHC and Future Colliders. *Symmetry* **2021**, *13*, 991. https://doi.org/10.3390/sym13060991

Academic Editors: Zoltán Trócsányi, Adam Kardos and Giuseppe Bevilacqua

Received: 27 April 2021
Accepted: 27 May 2021
Published: 2 June 2021

1. Introduction

The LHC discovery of a scalar particle consistent with the Standard Model (SM) predictions left many questions unanswered, among which is the lack of a dark matter candidate. This motivates investigations of beyond the SM extensions of the scalar sector. The Inert Doublet Model (IDM) [1–3], a Two Higgs Doublet Model with a discrete Z_2 symmetry, is a simple and well-motivated model that leads to a stable dark matter candidate. It has been discussed widely in the literature (see e.g., [4–50]), and we refer the reader to this discussion for further reference.

The imposed discrete Z_2 symmetry (called D-symmetry) corresponds to the following transformation properties:

$$\phi_S \to \phi_S, \ \phi_D \to -\phi_D, \ \text{SM} \to \text{SM}. \tag{1}$$

Here, the ϕ_S doublet plays the same role as the analogous doublet in the Standard Model, providing the SM-like Higgs particle. This doublet is even under the D-symmetry, while the second doublet, the inert (or dark) ϕ_D, is D-odd and contains four scalars, two charged and two neutral ones, labelled $H^\pm$ and H, A, respectively. In the rest of this work, we consider cases where H serves as the dark matter candidate of the model.

We refer here to our previous analysis [32,33,51], where we proposed benchmark scenarios with an emphasis on the discovery potential at e^+e^- colliders. The benchmarks presented in this work were chosen to cover a large range of the parameter space relevant at colliders, especially regarding the mass differences in the dark scalar sector. In particular, we divided the benchmark points into two categories, roughly split into areas where the new scalar masses are below 300 GeV or reach up to 500 GeV. As mass spectra are usually relatively degenerate for these particles [20,30,32], especially for higher masses $\gtrsim$ 300 GeV, all scalar masses are relatively close, so a characterization by one scale

is sufficient. For lower mass scales, the dark matter candidate can be lighter than the unstable scalars masses. Another important point is the on- or off-shellness of the decay products, which in this case are electroweak gauge bosons. As major backgrounds stem from the production of such bosons, together with missing energy, such features are an important selection criterium for signal over background enhancement. In total, we consider 40 specific parameter points, split into the low and high mass regions as discussed above. A more detailed description of the specific characteristics of these benchmark points is given in Section 4 below.

In this work cross-section predictions are given for these benchmarks, for a variety of production processes at the 13 and 27 TeV LHC, for a 100 TeV proton-proton collider, as well as for a muon collider. The unstable dark scalars decay as $A \to HZ\,(100\%)$ and $H^\pm \to W^\pm H$ (dominantly) for all points considered, where the above decays can be on- or off-shell depending on the mass spectra. Cross sections were calculated using Madgraph5 [52] with a UFO input file from [7]. Note the official version available at [53] exhibits a wrong CKM structure, leading to false results for processes involving electroweak gauge bosons radiated off quark lines. In our implementation, we corrected for this. Our implementation corresponds to the expressions available from [54].

In order to assess the possible collider reach, we then resort to a very simple counting criterium, and mark a benchmark point as reachable if at least 1000 events will have been produced for a specific collider scenario, using the colliders nominal center-of-mass energy and design luminosity. We acknowledge that this simple comparison criterium can only serve as a first step, and needs to be further tested by including full signal and background simulation, including the development of specific search strategies. However, we find this useful to provide first guidance for the benchmark points considered here.

The IDM is distinct in the sense that its unique signatures are mostly SM electroweak gauge boson and missing (transverse) energy. VBF-type SM scalar production with invisible decays in the off-shell mode is also an important channel, cf. for example, [34]. As couplings in both electroweak production and decay are determined by SM parameters (see e.g., discussion in [30]), rate predictions depend on a very small number of new physics parameters, typically mainly the masses of the new scalars; we will give examples to exceptions to this in the main body of this manuscript. This distinguishes it from other scalar extensions where a large number of additional parameters plays a role. While production modes can be similar to standard two Higgs doublet models, the exact Z_2 symmetry prevents couplings of the new scalars to fermions and therefore leads to distinct signatures of electroweak gauge bosons and missing (transverse) energy.

Finally, we want to briefly comment on other new physics models that lead to similar final states. In particular, many searches have been carried out by the LHC experiments within supersymmetric frameworks, cf. for example, [55,56]. Supersymmetric models can also lead to multilepton signatures and missing transverse energy. In [18,34], recasts of such searches within the IDM were considered. The parameter space in [18], which is excluded by LHC Run 1 searches is however equally excluded by dark matter considerations, as it features quite low dark matter masses which would lead to an overclosure of the universe. In [34], a heuristic argument was given why multilepton SUSY searches tend to cut out parameter regions in the IDM that would a priori lead to high event rates. Another model one could consider in this respect is the THDMa [57–63], a two Higgs Doublet model with an additional pseudoscalar that, in the gauge eigenstate, serves as a portal to a dark sector. Again, dilepton and missing transverse energy signatures are one of the prime channels of this model. However, both this and the SUSY scenarios come with topologies different to the one that led to these final states in the IDM. A more detailed comparison of the consequences of these differences is in the line of future work.

2. The IDM

The scalar sector of the IDM consists of two $SU(2)_L$ doublets of complex scalar fields, ϕ_S and ϕ_D, with the D-symmetric potential:

$$\begin{aligned} V = &-\tfrac{1}{2}\left[m_{11}^2(\phi_S^\dagger\phi_S)+m_{22}^2(\phi_D^\dagger\phi_D)\right] + \tfrac{\lambda_1}{2}(\phi_S^\dagger\phi_S)^2+\tfrac{\lambda_2}{2}(\phi_D^\dagger\phi_D)^2 \\ &+\lambda_3(\phi_S^\dagger\phi_S)(\phi_D^\dagger\phi_D)+\lambda_4(\phi_S^\dagger\phi_D)(\phi_D^\dagger\phi_S) + \tfrac{\lambda_5}{2}\left[(\phi_S^\dagger\phi_D)^2+(\phi_D^\dagger\phi_S)^2\right]. \end{aligned} \tag{2}$$

Exact D-symmetry (cf. Equation (1)) implies that only ϕ_S can acquire a nonzero vacuum expectation value (v). As a result the scalar fields from different doublets do not mix, and the lightest particle from ϕ_D is stable. The dark sector contains four new particles: H, A and $H^\pm$. We here choose H to denote the dark matter candidate (choosing A instead is equivalent to changing the sign of λ_5).

The model contains seven free parameters after electroweak symmetry breaking. The SM-like Higgs mass M_h and the vev, v, are fixed by LHC measurements as well as electroweak precision observables. We choose the remaining five free parameters to be

$$M_H, M_A, M_{H^\pm}, \lambda_2, \lambda_{345}, \tag{3}$$

where the λ's refer to couplings within the dark sector and to the SM-like Higgs, respectively, with $\lambda_{345} = \lambda_3 + \lambda_4 + \lambda_5$.

3. Experimental and Theoretical Constraints

We consider the following experimental and theoretical constraints on the model (see e.g., [20,32] for a more detailed discussion):

- Positivity constraints: we require that the potential is bounded from below.
- Perturbative unitarity: we require the scalar $2 \to 2$ scattering matrix to be unitary.
- Global minimum: in the IDM two neutral minima can coexist even at tree level. Unless the following relation is satisfied

$$\frac{m_{11}^2}{\sqrt{\lambda_1}} \geq \frac{m_{22}^2}{\sqrt{\lambda_2}}, \tag{4}$$

  the inert minimum is only a local one, with the global vacuum corresponding to the case of massless fermions [64]. We impose the above relation in our scan.
- Higgs mass and signal strengths: the mass of the SM-like Higgs boson h is set to

$$M_h = 125.1 \text{ GeV},$$

  in agreement with limits from ATLAS and CMS experiments [65,66], while the total width of the SM-like Higgs boson obeys an upper limit of [67]

$$\Gamma_{\text{tot}} \leq 9 \text{ MeV}. \tag{5}$$

  We have confirmed that all points obey the newest limit for invisible Higgs boson decays, $\text{BR}_{h\to\text{inv}} \leq 0.15$ [68]. Furthermore, all points have been checked against currently available signal strength measurements, including simplified template cross-section information, using the publicly available tool `HiggsSignals-2.6.0` [69,70], where we require agreement at 95% confidence level.
- Gauge bosons width: introduction of light new particles could in principle significantly change the total width of electroweak gauge bosons (cf. e.g., [54]). To ensure that $W^\pm \to HH^\pm$ and $Z \to HA, H^+H^-$ decay channels are kinematically forbidden we set:

$$M_{A,H} + M_{H^\pm} \geq M_W,\ M_A + M_H \geq M_Z,\ 2\,M_{H^\pm} \geq M_Z. \tag{6}$$

- Electroweak precision tests: we call for a $2\,\sigma$ (i.e., 95% C.L.) agreement with electroweak precision observables, parametrized through the electroweak oblique parameters S, T, U [71–74], tested against the latest results from the GFitter collaboration [75,76]. In our work, calculations were done through the routine implemented in the Two Higgs Doublet Model Calculator (`2HDMC`) tool [77], which checks whenever model predictions fall within the observed parameter range.
- Charged scalar mass and lifetime: we take a conservative lower estimate on the mass of $M_{H^\pm}$ following analysis in [78] to be

$$M_{H^\pm} \geq 70 \text{ GeV}. \tag{7}$$

We also set an upper limit on the charged scalar lifetime of

$$\tau \leq 10^{-7}\, s, \tag{8}$$

in order to evade bounds from quasi-stable charged particle searches. More detailed studies using recasts of current LHC long-lived particle searches can be found in [79,80].
- Collider searches for new physics: we require agreement with the null-searches from the LEP, Tevatron, and LHC experiments. We use the publicly available tool `HiggsBounds-5.9.0` [81–85]. In addition the reinterpreted LEP II searches for supersymmetric particles analysis exclude the region of masses in the IDM where simultaneously [8]

$$M_A \leq 100 \text{ GeV}, M_H \leq 80 \text{ GeV}, \Delta M(A,H) \geq 8 \text{ GeV}, \tag{9}$$

as it would lead to a visible di-jet or dilepton signal. After taking into account all the above limits we are outside of the region excluded due to the reinterpretation of the supersymmetry analysis from LHC Run I [18].
- Dark matter phenomenology: we apply dark matter relic density limits obtained by the Planck experiment [86]:

$$\Omega_c\, h^2 = 0.1200 \pm 0.0012. \tag{10}$$

For a DM candidate that provides 100% of observed DM in the Universe we require the above bound to be fulfilled within the 2σ limit. However, we also allow for the case where H is only a subdominant DM candidate, with

$$\Omega_H h^2 < \Omega_c\, h^2. \tag{11}$$

Note that this also leads to a rescaling of the respective direct detection limits [20,32]. In the results presented here, we apply XENON1T limits [87]. We use a digitized format of that data available from [88]. For consistency, we here calculated the dark-matter related variables using `micrOMEGAs_5.0.4` [89]. Note that for some points, relic density values change using the most up-to-date version, that is, `micrOMEGAs_5.2.4` [90]. Similar results can be obtained by changing the integration mode for some points. We list the corresponding values for the low-mass benchmark points in Appendix A for reference.

3.1. Requiring Exact Relic Density

As discussed above, we here require relic density to be below the current value as determined by the Planck collaboration (cf. Equation (10)). In the Inert Doublet model, meeting the exact relic density is only possible in certain mass ranges. We here enhance a previous discussion on this which was presented in [32] (see also the discussion in [91]).

- **Lower bound on dark matter mass**
  A combination of signal strength measurements for the 125 GeV resonance sets an upper limit on the absolute value of the coupling λ_{345}, which determines the HHh coupling. In this area, the major annihilation channel is $HH \to b\bar{b}$, mediated by h-exchange. Low values of λ_{345} in turn lead to large values for the relic density, as annihilation cross sections are taking lower values. In principle, co-annihilation with A or $H^\pm$ could remedy this, leading to larger annihilation cross sections, for mass splittings which are smallish. Indeed, in [91] this scenario is explicitly discussed (see also [6]). The combination of these bounds leads to a lowest value of $M_H \sim 55$ GeV [20,30,34,91]. In a more detailed scan, however, we find that masses can in principle be as low as around 44 GeV, if the mass difference between M_A and M_H is quite small, up to 4 GeV; the dominant contribution then comes from coannihilation of $HA \to \left(d\bar{d}, s\bar{s}, b\bar{b}\right)$, but none of these points results in the correct relic density.
- **Resonance region, $M_H \sim M_h/2$**
  In this region, the main annihilation channels are h-mediated, primarily into $b\bar{b}$ and W^+W^- final states. This leads to points that meet the exact relic density, with smallish $|\lambda_{345}| \lesssim 0.006$ values.
- **Region up to around 75 GeV**
  In this region, HH annihilation into (partially off-shell) W^+W^- final states start to dominate. Due to interference effects between h-mediated and quartic couplings (see e.g., [5,91]), some points in the mass range around $70 - 73$ GeV render exact relic density, including all current constraints. Absolute values for λ_{345} are $\lesssim 0.006$ in that region. As in the low mass region, for quite mass-degenerate scalars, $M_H - M_A \lesssim 7$ GeV, the dominant annihilation process is given by $HA \to \left(d\bar{d}, s\bar{s}, b\bar{b}\right)$; none of these points however renders the correct relic density.
- **Region between 75 GeV and 160 GeV**
  This region was proposed in [92] as a good region for dark matter relic density in the IDM, where the calculation depends on cancellations between diagrams for VV^* final states. However, the values for λ_{345} required here are by now ruled out by limits from direct detection experiments. The dominant annihilation channel is $HH \to W^+W^-$.
- **Region between 160 GeV and around 500 GeV**
  In this region, currently no study exists that provides scenarios within the IDM where exact relic density can be generated. Examples for studies are given in [7,13,20]. Largest values of relic density stem from $HH \to W^+W^-$ annihilation, with annihiliation rates too large to render the exact value.
- **Larger masses, $M_H \gtrsim 500$ GeV**
  Here, the exact values of relic density can be obtained if mass splittings between dark scalars are quite small, roughly $\lesssim 10$ GeV (see also discussion in [93]). The dominant annihilation channel is $HH \to W^+W^-$. It is possible to obtain the correct relic density for small mass differences $M_{H^\pm} - M_H \lesssim 10$ GeV, $|\lambda_{345}| \lesssim 0.25$.

4. Benchmark Points

In this section, we list all production cross sections for the production channels

$$pp \to HA,\ HH^+,\ HH^-,\ AH^+,\ AH^-,\ H^+H^-,\ AA \tag{12}$$

for the benchmark scenarios proposed in [32], for center-of-mass energies of 13 and 27 TeV and 100 TeV proton-proton collider. We additionally consider the VBF-like production of AA and H^+H^- at the same hadron collider options as well as a muon-muon collider with center of mass energies of 10 TeV and 30 TeV. Cross sections were calculated using Madgraph5 [52], with an UFO input model from [7]. We separate the benchmarks into low mass benchmark points (BPs) with dark masses up to 300 GeV, as well as high mass points (HPs), which cover the whole mass range up to 1 TeV. The parameter choices as well as kinetic properties of these points are listed in Tables 1 and 2. We also emphasize when a point reproduces exact relic density.

Table 1. In all benchmarks $M_h = 125.1$ GeV. Bold font denotes BP with 100% DM relic density. Note that BP5 and BP17 were excluded by the updated XENON1T limits [87]. Taken from [32], with adjustments for λ_{345} as discussed in [33] and updated relic density values using `micOMEGAS_5.0.4`.

No.	M_H	M_A	$M_{H^\pm}$	Z on-shell	W on-shell	DM >50%	λ_2	λ_{345}	$\Omega_H h^2$
BP1	72.77	107.803	114.639			✓	1.44513	−0.00440723	0.11998
BP2	65	71.525	112.85			✓	0.779115	0.0004	0.07076
BP3	67.07	73.222	96.73			✓	0	0.00738	0.06159
BP4	73.68	100.112	145.728			✓	2.08602	−0.00440723	0.089114
BP6	72.14	109.548	154.761		✓	✓	0.0125664	−0.00234	0.117
BP7	76.55	134.563	174.367		✓		1.94779	0.0044	0.031381
BP8	70.91	148.664	175.89		✓	✓	0.439823	0.0058	0.12207
BP9	56.78	166.22	178.24	✓	✓	✓	0.502655	0.00338	0.081243
BP23	62.69	162.397	190.822	✓	✓	✓	2.63894	0.0056	0.065
BP10	76.69	154.579	163.045		✓		3.92071	0.0096	0.028125
BP11	98.88	155.037	155.438				1.18124	−0.0628	0.002735
BP12	58.31	171.148	172.96	✓	✓		0.540354	0.00762	0.0064104
BP13	99.65	138.484	181.321		✓		2.46301	0.0532	0.0012541
BP14	71.03	165.604	175.971	✓	✓	✓	0.339292	0.00596	0.11833
BP15	71.03	217.656	218.738	✓	✓	✓	0.766549	0.00214	0.12217
BP16	71.33	203.796	229.092	✓	✓	✓	1.03044	−0.00122	0.12205
BP18	147	194.647	197.403				0.387	−0.018	0.0017711
BP19	165.8	190.082	195.999				2.7675	−0.004	0.0028308
BP20	191.8	198.376	199.721				1.5075	0.008	0.0084219
BP21	57.475	288.031	299.536	✓	✓	✓	0.929911	0.00192	0.11942
BP22	71.42	247.224	258.382	✓	✓	✓	1.04301	−0.0032	0.12206

Table 2. High-mass benchmark points (HPs) accessible at colliders with $\mathcal{O}(\text{TeV})$ center-of-mass energies. $M_h = 125.1\,\text{GeV}$ for all points. HP10 provides exact relic density. Taken from [32], with adjustments for λ_{345} as discussed in [33] and updated relic density values using `micOMEGAS_5.0.4`.

No.	M_H	M_A	$M_{H^\pm}$	Z on-shell	W on-shell	DM >50%	λ_2	λ_{345}	$\Omega_H h^2$
HP1	176	291.36	311.96	✓	✓		1.4895	−0.1035	0.00072692
HP2	557	562.316	565.417			✓	4.0455	−0.1385	0.07163
HP3	560	616.32	633.48				3.3795	−0.0895	0.0011357
HP4	571	676.534	682.54	✓	✓		1.98	−0.471	0.00056712
HP5	671	688.108	688.437				1.377	−0.1455	0.024523
HP6	713	716.444	723.045				2.88	0.2885	0.035145
HP7	807	813.369	818.001				3.6675	0.299	0.032488
HP8	933	939.968	943.787			✓	2.9745	−0.2435	0.09637
HP9	935	986.22	987.975				2.484	−0.5795	0.0028109
HP10	990	992.36	998.12			✓	3.3345	−0.040	0.12215
HP11	250.5	265.49	287.226				3.90814	−0.150071	0.0053534
HP12	286.05	294.617	332.457				3.29239	0.112124	0.002771
HP13	336	353.264	360.568				2.48814	−0.106372	0.009366
HP14	326.55	331.938	381.773				0.0251327	−0.0626727	0.0035646
HP15	357.6	399.998	402.568				2.06088	−0.237469	0.0034553
HP16	387.75	406.118	413.464				0.816814	−0.208336	0.01158
HP17	430.95	433.226	440.624				3.00336	0.082991	0.032697
HP18	428.25	453.979	459.696				3.87044	−0.281168	0.0085817
HP19	467.85	488.604	492.329				4.12177	−0.252036	0.013879
HP20	505.2	516.58	543.794				2.53841	−0.354	0.0088693

Figure 1 shows the initial benchmark candidates discussed in [32], that obey all current constraints, in the $(M_{H^+} - M_H; M_A - M_H)$ plane. All points form a narrow band corresponding to $M_A \lesssim M_{H^\pm}$. Our chosen benchmark points, also indicated in Figure 1 (red points) cover mass gaps up to about 250 GeV.

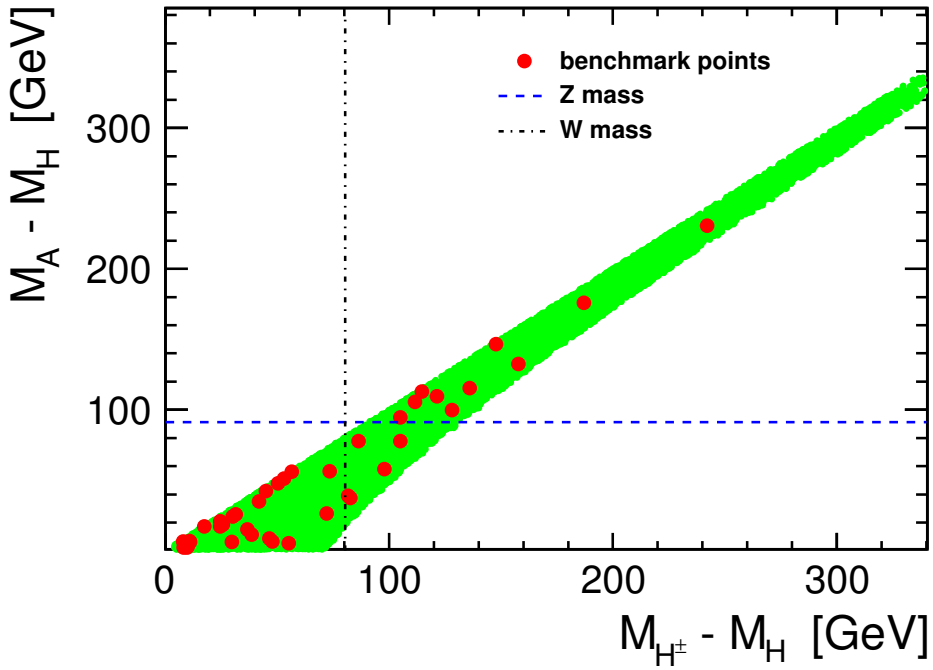

Figure 1. Distribution of benchmark candidate points (green) in the $(M_{H^+} - M_H; M_A - M_H)$ plane, after all constraints are taken into account, as well as selected benchmark points (red) in the same plane. The dashed lines indicate the electroweak gauge boson masses that distinguish between on- and off-shell decays of dark scalars. The relatively narrow band stems mainly from electroweak precision constraints. Plot was shown previously in [32].

5. Production Cross Sections at Various Collider Options

We first focus on the completed LHC Run 2 with a center-of-mass energy of 13 TeV and assuming an integrated luminosity of 150 fb^{-1}. The production cross sections at 13 TeV for all considered benchmark scenarios are listed in Tables 3 and 4. In Figure 2 cross sections for different on-shell scalar pair-production channels are compared, shown as a function of the sum of produced scalar masses. We note that, apart from AA production, all processes show a similar decrease in the cross section as the mass scale rises; as these production modes are stemming from Drell-Yan processes with intermediate gauge bosons, the masses remain the only undetermined parameters, while all couplings are given by SM electroweak variables. Therefore, differences between, for example, HH^+ and AH^+ are small for the same mass scale. In general, AH^-/HH^- states are produced with slightly lower cross sections, due to the parton content of the proton. For the AA process, however, the coupling

$$\bar{\lambda}_{345} \equiv \lambda_3 + \lambda_4 - \lambda_5 = \lambda_{345} - 2\,\frac{M_H^2 - M_A^2}{v^2} \tag{13}$$

determines the cross section, which is no longer a function of the mass only. Therefore, for this production mode the cross sections do not follow the same simple behaviour. For example, cross sections $\lesssim 0.1$ fb are usually achieved for $\bar{\lambda}_{345} \lesssim 0.5$ for the low mass BPs.

Table 3. Production cross sections in fb for low-mass benchmark points from Table 1, for different on-shell scalar pair-production channels at 13 TeV LHC. Bold font denotes benchmark points for which H completely saturates DM relic density.

No.	M_H	M_A	$M_{H^\pm}$	HA	$H\,H^+$	$H\,H^-$	AH^+	$A\,H^-$	H^+H^-	AA
BP1	72.77	107.803	114.639	322	304	183	169	98.2	133	0.925
BP2	65	71.525	112.85	1020	363	220	323	195	141	1.46
BP3	67.07	73.222	96.73	909	505	311	444	272	243	0.939
BP4	73.68	100.112	145.728	377	166	96.4	115	65.7	56.3	0.757
BP6	72.14	109.548	154.761	314	144	83.5	90.0	50.0	45.5	0.912
BP7	76.55	134.563	174.367	173	99.1	56.2	50.9	27.7	29.3	0.491
BP8	70.91	148.664	175.89	144	103	58.6	42.8	23.0	28.6	0.500
BP9	56.78	166.22	178.24	125	116	66.4	34.5	18.3	27.3	0.683
BP10	76.69	154.579	163.045	120	119	67.8	46.4	25.2	37.3	0.489
BP11	98.88	155.037	155.438	87.7	101	57.2	50.5	27.5	44.0	0.278
BP12	58.31	171.148	172.96	113	125	71.7	34.6	18.4	30.3	0.554
BP13	99.65	138.484	181.321	113	68.8	38.2	44.9	24.2	25.0	0.209
BP14	71.03	165.604	175.971	106	103	58.5	35.6	18.9	28.6	0.650
BP15	71.03	217.656	218.738	46.9	54.6	30.0	14.2	7.14	12.9	0.502
BP16	71.33	203.796	229.092	57.3	47.3	25.8	14.6	7.36	10.9	0.536
BP18	147	194.647	197.403	29.2	34.0	18.1	21.3	11.0	17.9	0.112
BP19	165.8	190.082	195.999	25.2	28.6	15.0	22.6	11.7	18.3	0.0362
BP20	191.8	198.376	199.721	17.7	21.4	11.0	20.1	10.3	16.9	0.00305
BP21	57.475	288.031	299.536	20.6	21.8	11.4	4.44	2.06	4.09	0.345
BP22	71.42	247.224	258.382	31.3	32.5	17.3	8.04	3.89	7.00	0.381
BP23	62.69	162.397	190.822	125	88.9	50.2	31.3	16.5	21.1	0.545

Table 4. Production cross sections in fb for high-mass benchmark points from Table 2, for different on-shell scalar pair-production channels at the 13 TeV LHC. Dashes (-) indicate cross-section values smaller than 10^{-3} fb. For the HP10 scenario (bold) H completely saturates DM relic density.

No.	M_H	M_A	$M_{H^\pm}$	HA	$H\,H^+$	$H\,H^-$	AH^+	AH^-	H^+H^-	AA
HP1	176	291.36	311.96	8.33	8.76	4.27	3.99	1.84	3.12	0.132
HP2	557	562.316	565.417	0.184	0.259	0.0993	0.253	0.0970	0.190	-
HP3	560	616.32	633.48	0.143	0.191	0.0718	0.153	0.0565	0.115	0.00273
HP4	571	676.534	682.54	0.105	0.149	0.0552	0.0991	0.0358	0.0830	0.00512
HP5	671	688.108	688.437	0.0672	0.0990	0.0358	0.0927	0.0334	0.0690	-
HP6	713	716.444	723.045	0.0511	0.0740	0.0263	0.0730	0.0260	0.0529	-
HP7	807	813.369	818.001	0.0253	0.0375	0.0129	0.0367	0.0126	0.0265	-
HP8	933	939.968	943.787	0.0106	0.0161	0.00530	0.0157	0.00518	0.0113	-
HP9	935	986.22	987.975	0.00904	0.0139	0.00453	0.0118	0.00383	0.00883	-
HP10	990	992.36	998.12	0.00742	0.0113	0.00366	0.0112	0.00363	0.00794	-
HP11	250.5	265.49	287.226	5.82	6.30	3.00	5.66	2.68	4.03	-
HP12	286.05	294.617	332.457	3.59	3.60	1.64	3.41	1.56	2.23	0.00337
HP13	336	353.264	360.568	1.73	2.21	0.977	1.99	0.874	1.54	0.00135
HP14	326.55	331.938	381.773	2.11	2.05	0.902	1.99	0.872	1.23	-
HP15	357.6	399.998	402.568	1.14	1.52	0.655	1.21	0.512	0.955	0.00556
HP16	387.75	406.118	413.464	0.931	1.21	0.515	1.10	0.464	0.840	-
HP17	430.95	433.226	440.624	0.632	0.837	0.347	0.828	0.342	0.627	-
HP18	428.25	453.979	459.696	0.575	0.769	0.318	0.678	0.276	0.517	-
HP19	467.85	488.604	492.329	0.394	0.541	0.217	0.490	0.196	0.374	-
HP20	505.2	516.58	543.794	0.287	0.357	0.140	0.340	0.132	0.233	-

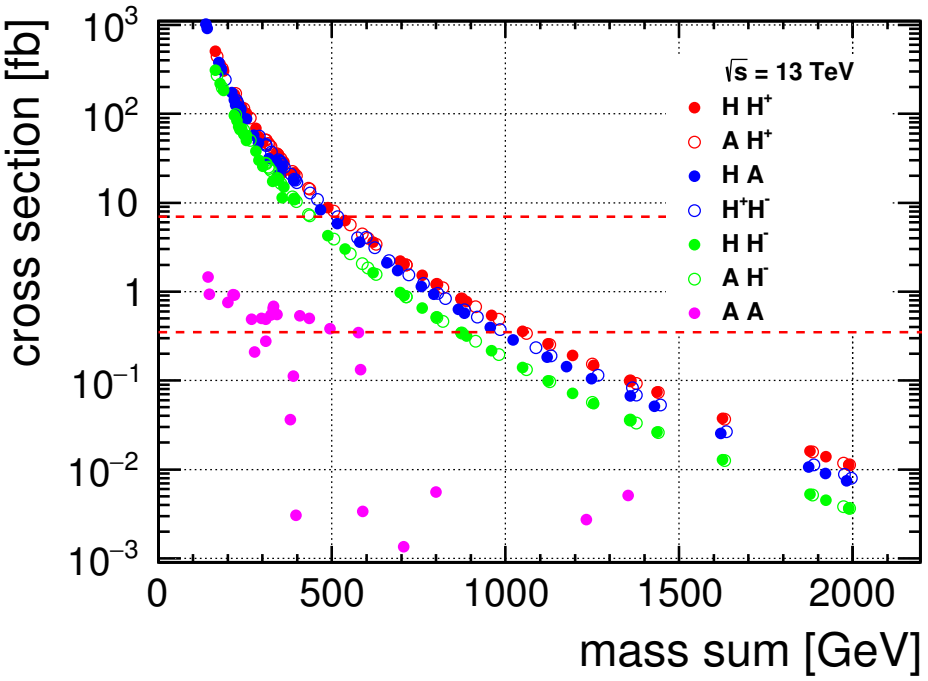

Figure 2. Production cross sections for benchmarks from Tables 1 and 2 as a function of the produced scalar mass sum, for on-shell scalar pair-production at 13 TeV LHC. Horizontal dashed lines indicate minimal cross sections required to produce 1000 events at LHC Run 2 and HL-LHC (see text for details).

We label scenarios as realistic, if they produce at least 1000 events during that run, translating to minimal cross sections of about 7 fb indicated by the horizontal dashed line in Figure 2. We note that this only corresponds to a rough estimate of accessibility. Detailed studies, including background simulation, would be needed to determine discovery options for each BP individually. Note that the decays of the heavier dark scalars are predominantly given by

$$H^\pm \to W^\pm H; A \to Z H,$$

with the electroweak gauge bosons decaying as in the SM. Only BPs 2,3,4 have sizeable branching ratios for the channel $H^\pm \to A W^\pm$ of 0.34, 0.25, and 0.08, respectively.

5.1. Current LHC Data, Run 2

With the simple counting criterium proposed above, one can see that minimum cross section of 7 fb (horizontal dashed line in Figure 2) limits the LHC Run 2 sensitivity to the scalar mass sum of about 450 GeV for HH^- and AH^- production channels and to about 500 GeV for other scalar pair-production channels. We see that most of the low mass benchmark points in Table 3 (BPs 1-16, 18-20 as well as 23) provide high enough cross sections for dark scalar pair-production in all channels but the AA pair-production channel. On the other hand, for the high-mass benchmark points (Table 4), only HP 1 renders high enough cross sections in the HA and HH^+ production mode.

5.2. High Luminosity Option

At the high luminosity LHC, the target integrated luminosity corresponds to 3 ab^{-1} (see e.g., [94]), lowering the cross-section threshold for our simple counting criterium to 0.33 fb. The accessible mass range for pair-production of IDM scalars is extended to a mass sum of about 850 GeV for HH^- and AH^- channel, and about 1 TeV for other channels (except for AA), see Figure 2. The AA channel additionally opens up for BPs 1-10, 12, 14-17, and 23. Similarly BP21 and 22 also render the minimal number of generated events in all channels. Only for BPs 11, 13, and 18-20 the total number of events generated

does not suffice in the AA channel. Note that the hAA coupling scales with $\bar{\lambda}_{345}$, cf. Equation (13). For the high-mass points, now HP1, HP11-16 become accessible in all but the AA channel; for HPs 17-19, the $HA, H, H H^+, A H^+, H^+ H^-$ channels seem to become accessible, corresponding to a mass range for scalar masses up to 500 GeV.

5.3. High Energy Option

Values for the production cross sections at a 27 TeV center-of-mass energy are given in Tables 5 and 6. With a center-of-mass energy of 27 TeV and a target luminosity of 15 ab^{-1} [95], the minimal cross section required to obtain at least 1000 events in the full run further decreases to 0.07 fb. This means that all but BP20 are accessible in all channels. BP20 features a low value of $\bar{\lambda}_{345} \sim 0.09$ and a relatively high mass M_A, leading to a low AA cross section even at the 27 TeV HE-LHC. For the high-mass points, HPs 2-7, 11-20 are open in all but the AA channel, while HP1 even renders a large enough cross section for this channel as well. For HPs 8-10, the $H H^-, A H^-$ channels additionally remain inaccessible. This means that all HPs and BPs are accessible in at least one channel, with scalar masses up to 1 TeV. The enhancement factors for production processes with respect to cross sections at the LHC including at least one unstable new scalar are shown in Figure 3. In general, for the low BPs the cross-section enhancement is about a factor 3, where for AA final states a maximal value of ~ 6 is reached for BP21. For HPs the enhancement can be up to a factor 10 depending on the dark scalar masses. In fact, the largest enhancement is obtained for HP10, where the cross section increases by a factor 20. However, the absolute value for AA production at 27 TeV for this point is $\mathcal{O}(10^{-6}\,\text{fb})$, making it too small for a detailed investigation of this channel.

Table 5. Production cross sections for BPs from Table 1 in fb for for on-shell scalar pair-production at 27 TeV HE-LHC.

No.	M_H	M_A	$M_{H^\pm}$	HA	$H H^+$	$H H^-$	AH^+	$A H^-$	H^+H^-	AA
BP1	72.77	107.803	114.639	846	770	516	441	289	368	3.84
BP2	65	71.525	112.85	2540	910	614	814	547	387	5.23
BP3	67.07	73.222	96.73	2270	1250	849	1100	750	645	3.39
BP4	73.68	100.112	145.728	982	432	284	308	199	166	3.06
BP6	72.14	109.548	154.761	824	380	248	241	154	137	3.81
BP7	76.55	134.563	174.367	470	266	172	143	89.4	91.7	2.22
BP8	70.91	148.664	175.89	396	276	178	122	75.5	90.5	2.34
BP9	56.78	166.22	178.24	347	309	200	100	61.2	87.0	3.35
BP10	76.69	154.579	163.045	332	316	205	131	81.9	114	2.33
BP11	98.88	155.037	155.438	249	271	175	142	88.8	131	1.33
BP12	58.31	171.148	172.96	313	331	215	100	61.5	94.7	2.76
BP13	99.65	138.484	181.321	316	189	120	127	79.0	79.1	0.954
BP14	71.03	165.604	175.971	297	276	178	103	63.1	90.3	3.19
BP15	71.03	217.656	218.738	138	152	95.6	44.3	26.0	45.0	2.78
BP16	71.33	203.796	229.092	167	133	83.2	45.4	26.8	38.9	2.87
BP18	147	194.647	197.403	89.6	98.5	60.4	64.0	38.4	57.8	0.590
BP19	165.8	190.082	195.999	78.4	83.9	51.1	67.5	40.6	58.5	0.188
BP20	191.8	198.376	199.721	56.7	64.3	38.6	60.7	36.4	54.4	0.0161
BP21	57.475	288.031	299.536	64.6	65.0	39.2	15.5	8.62	17.5	2.21
BP22	71.42	247.224	258.382	94.9	94.0	57.8	26.4	15.1	26.9	2.25
BP23	62.69	162.397	190.822	348	241	154	91.2	55.9	69.3	2.66

Table 6. Production cross sections for HPs from Table 2 in fb for high-mass benchmark points for scalar pair-production at the 27 TeV HE-LHC.

No.	M_H	M_A	$M_{H^\pm}$	HA	$H\,H^+$	HH^-	AH^+	AH^-	H^+H^-	AA
HP1	176	291.36	311.96	28.7	28.5	16.4	14.1	7.79	12.9	0.850
HP2	557	562.316	565.417	1.07	1.36	0.650	1.34	0.637	1.11	-
HP3	560	616.32	633.48	0.871	1.06	0.498	0.886	0.410	0.787	0.0311
HP4	571	676.534	682.54	0.678	0.871	0.402	0.630	0.284	0.642	0.0644
HP5	671	688.108	688.437	0.474	0.629	0.284	0.598	0.269	0.488	0.00151
HP6	713	716.444	723.045	0.381	0.499	0.222	0.494	0.220	0.395	-
HP7	807	813.369	818.001	0.219	0.294	0.126	0.289	0.123	0.230	-
HP8	933	939.968	943.787	0.113	0.155	0.0634	0.152	0.0623	0.118	-
HP9	935	986.22	987.975	0.0999	0.138	0.0563	0.123	0.0496	0.103	0.00364
HP10	990	992.36	998.12	0.0861	0.119	0.0479	0.118	0.0476	0.0910	-
HP11	250.5	265.49	287.226	20.9	21.2	12.0	19.3	10.8	15.1	0.00521
HP12	286.05	294.617	332.457	13.6	12.9	7.07	12.3	6.72	9.09	0.0219
HP13	336	353.264	360.568	7.18	8.39	4.49	7.67	4.08	6.49	0.00980
HP14	326.55	331.938	381.773	8.53	7.86	4.19	7.65	4.07	5.43	-
HP15	357.6	399.998	402.568	5.00	6.07	3.19	4.97	2.57	4.35	0.0440
HP16	387.75	406.118	413.464	4.20	5.00	2.59	4.60	2.37	3.85	0.00448
HP17	430.95	433.226	440.624	3.02	3.64	1.85	3.61	1.83	3.01	-
HP18	428.25	453.979	459.696	2.78	3.39	1.72	3.05	1.53	2.57	0.00756
HP19	467.85	488.604	492.329	2.02	2.52	1.25	2.32	1.14	1.95	0.00385
HP20	505.2	516.58	543.794	1.55	1.78	0.862	1.71	0.824	1.32	-

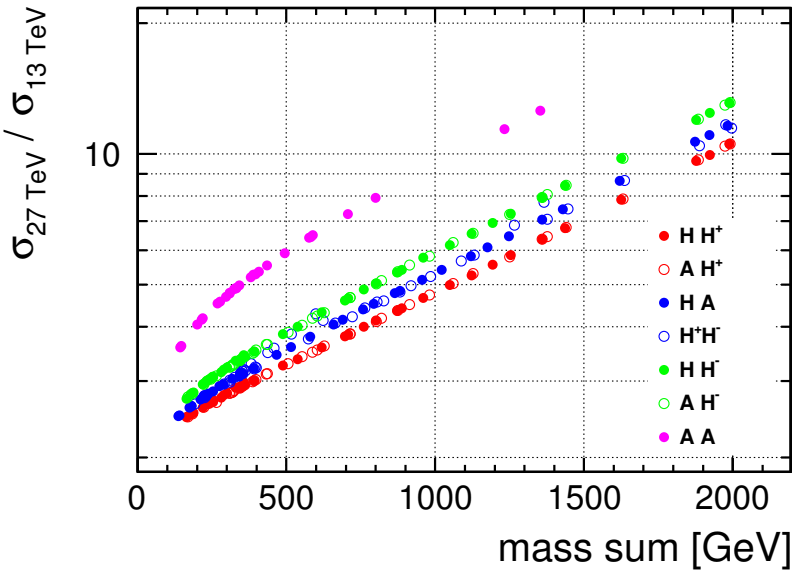

Figure 3. Ratio of production cross sections for all production channels specified with at least one unstable new scalar at the 27 TeV HE-LHC and current center-of-mass energy of 13 TeV. While in the low energy range, cross sections are enhanced roughly by a factor $\lesssim 3$, for higher masses they can change by an order of magnitude. Scenarios with cross-section value smaller than 10^{-3} fb at 13 TeV are not indicated.

5.4. 100 TeV Proton-Proton Collider

A circular hadron–hadron collider with a 100 TeV center of mass energy is currently another option for a future accelerator design [96,97]. For reference, we therefore list the corresponding cross-sections for scalar pair-production in Tables 7 and 8. The target accelerator luminosity corresponds to 20 ab^{-1}; this corresponds to a production cross section of 5×10^{-2} fb, respectively, to fulfill our accessibility criterium.

For the low BPs, this would allow closure of the remaining AA channel for BP 20. For the high-mass benchmark points, HPs 1, 3, 4, 9, 11-13, 15, 16, 18, 19 now could be reachable

in all channels using our criterium. For the remaining points, the AA production cross section remains too low. As for the HE-LHC, this corresponds to a possible mass reach up to 1 TeV for the single scalar masses, where, however, a larger number of total channels is open.

Table 7. Production cross sections for BPs from Table 1 in pb for for on-shell scalar pair-production at a 100 TeV FCC.

No.	M_H	M_A	$M_{H^\pm}$	HA	$H\,H^+$	$H\,H^-$	AH^+	$A\,H^-$	H^+H^-	AA
BP1	72.77	107.803	114.639	4.00	3.47	2.65	2.06	1.55	1.85	0.0337
BP2	65	71.525	112.85	11.2	4.07	3.12	3.67	2.80	1.94	0.0380
BP3	67.07	73.222	96.73	10.1	5.47	4.22	4.88	3.75	3.09	0.0249
BP4	73.68	100.112	145.728	4.61	2.02	1.52	1.47	1.10	0.901	0.0260
BP6	72.14	109.548	154.761	3.91	1.79	1.34	1.17	0.871	0.763	0.0336
BP7	76.55	134.563	174.367	2.31	1.29	0.957	0.722	0.529	0.530	0.0215
BP8	70.91	148.664	175.89	1.97	1.33	0.992	0.622	0.453	0.533	0.0238
BP9	56.78	166.22	178.24	1.74	1.47	1.10	0.517	0.375	0.517	0.0359
BP10	76.69	154.579	163.045	1.67	1.51	1.13	0.668	0.488	0.641	0.0241
BP11	98.88	155.037	155.438	1.28	1.31	0.975	0.718	0.525	0.715	0.0137
BP12	58.31	171.148	172.96	1.58	1.57	1.18	0.519	0.376	0.550	0.0299
BP13	99.65	138.484	181.321	1.60	0.937	0.691	0.647	0.472	0.459	0.00938
BP14	71.03	165.604	175.971	1.51	1.33	0.989	0.531	0.385	0.532	0.0341
BP15	71.03	217.656	218.738	0.742	0.763	0.560	0.244	0.173	0.301	0.0341
BP16	71.33	203.796	229.092	0.882	0.674	0.493	0.250	0.177	0.268	0.0341
BP18	147	194.647	197.403	0.499	0.511	0.370	0.343	0.246	0.337	0.00685
BP19	165.8	190.082	195.999	0.441	0.441	0.318	0.361	0.259	0.336	0.00216
BP20	191.8	198.376	199.721	0.329	0.345	0.247	0.327	0.234	0.311	0.000189
BP21	57.475	288.031	299.536	0.367	0.346	0.249	0.0941	0.0646	0.153	0.0319
BP22	71.42	247.224	258.382	0.524	0.487	0.353	0.152	0.106	0.204	0.0296
BP23	62.69	162.397	190.822	1.74	1.17	0.867	0.476	0.345	0.425	0.0280

Table 8. Production cross sections for HPs from Table 2 in fb for high-mass benchmark points for scalar pair-production at a 100 TeV FCC.

No.	M_H	M_A	$M_{H^\pm}$	HA	$H\,H^+$	$H\,H^-$	AH^+	$A\,H^-$	H^+H^-	AA
HP1	176	291.36	311.96	176	163	114	86.4	59.2	103	12.3
HP2	557	562.316	565.417	9.89	11.1	7.00	10.9	6.88	10.1	-
HP3	560	616.32	633.48	8.32	9.01	5.62	7.72	4.77	9.27	0.781
HP4	571	676.534	682.54	6.76	7.60	4.70	5.79	3.53	9.13	1.76
HP5	671	688.108	688.437	5.02	5.78	3.52	5.54	3.37	5.19	0.0421
HP6	713	716.444	723.045	4.21	4.79	2.89	4.75	2.86	4.39	0.0185
HP7	807	813.369	818.001	2.69	3.11	1.84	3.07	1.81	2.85	0.0210
HP8	933	939.968	943.787	1.59	1.87	1.07	1.85	1.06	1.66	-
HP9	935	986.22	987.975	1.45	1.71	0.978	1.56	0.886	1.72	0.150
HP10	990	992.36	998.12	1.29	1.52	0.863	1.52	0.856	1.36	-
HP11	250.5	265.49	287.226	132	125	86.6	115	79.2	99.1	0.0714
HP12	286.05	294.617	332.457	89.9	79.5	54.3	76.1	51.9	65.6	0.320
HP13	336	353.264	360.568	51.0	54.2	36.4	50.1	33.6	46.7	0.160
HP14	326.55	331.938	381.773	59.4	51.2	34.3	49.9	33.5	42.2	0.00751
HP15	357.6	399.998	402.568	37.2	40.7	27.0	34.1	22.5	33.7	0.781
HP16	387.75	406.118	413.464	31.8	34.3	22.6	31.8	20.9	29.6	0.0805
HP17	430.95	433.226	440.624	23.9	26.0	17.0	25.7	16.8	23.7	0.0180
HP18	428.25	453.979	459.696	22.3	24.4	15.9	22.2	14.4	20.9	0.147
HP19	467.85	488.604	492.329	16.9	18.8	12.1	17.5	11.2	16.5	0.0795
HP20	505.2	516.58	543.794	13.5	14.0	8.87	13.5	8.54	12.1	-

Production cross sections for selected scalar pair-production channels, for different proton collider options, are compared in Figure 4. In general, production cross sections are enhanced by one to two orders of magnitude with respect to the corresponding values at the 13 TeV LHC, cf. Figure 5.

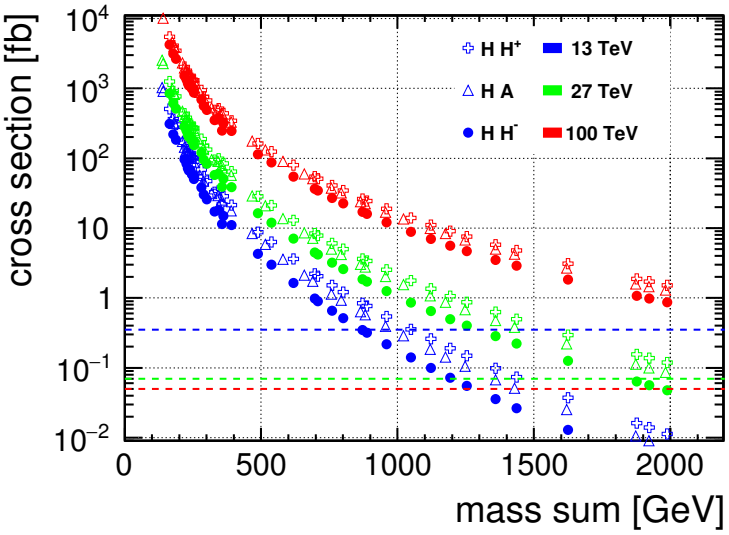

Figure 4. Production cross sections for benchmarks from Tables 1 and 2 as a function of the produced scalar mass sum, for selected scalar pair-production channels, for 13 TeV, 27 TeV and 100 TeV proton collider options. Horizontal dashed lines indicate minimal cross sections required to produce 1000 events at the respective energy, assuming design luminosity.

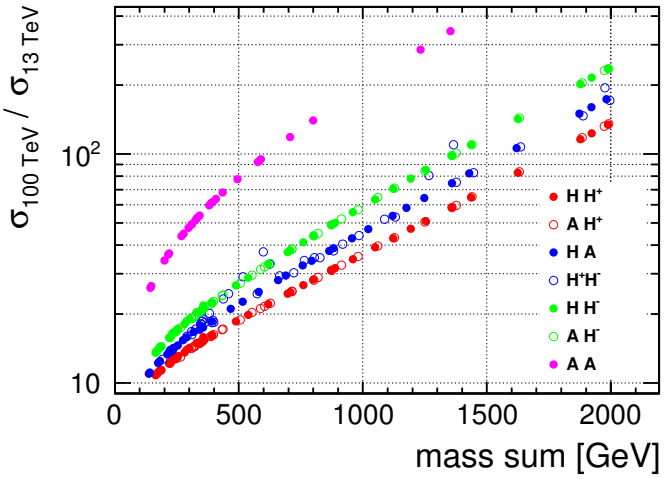

Figure 5. Ratio of production cross sections for all production channels specified with at least one unstable new scalar at the 100 TeV pp collider and the LHC with a center-of-mass energy of 13 TeV. Production cross sections are enhanced roughly by one to two orders of magnitude.

5.5. VBF-Like Topologies

Apart from the direct pair-production processes in Equation (12), also final states with additional jets should be considered. We here include all processes that lead to the required final state; a subset of these are VBF-like topologies. As an example, we additionally consider

$$p\,p \to A\,A\,j\,j,\; p\,p \to H^+\,H^-\,j\,j.$$

Both processes can include VBF-type diagrams. The respective cross sections for the low and high mass benchmarks, with varying collider energies, are given in Tables 9 and 10, and compared in Figure 6.

Table 9. Production cross sections for BPs from Table 1 in fb for X + dijet at proton-proton colliders for varying center-of-mass energies. No VBF cuts were applied.

No.	M_H	M_A	$M_{H^\pm}$	$(AA)_{13}$	$(AA)_{27}$	$(AA)_{100}$	$(H^+H^-)_{13}$	$(H^+H^-)_{27}$	$(H^+H^-)_{100}$
BP1	72.77	107.803	114.639	0.750	3.11	27.5	33.5	137	1070
BP2	65	71.525	112.85	18.9	52.0	250	34.8	142	1120
BP3	67.07	73.222	96.73	3.87	11.1	58.9	55.5	217	1660
BP4	73.68	100.112	145.728	2.99	9.44	56.5	16.0	70.9	606
BP6	72.14	109.548	154.761	1.33	5.02	38.0	13.5	61.4	536
BP7	76.55	134.563	174.367	0.988	4.43	42.5	9.22	43.5	420
BP8	70.91	148.664	175.89	0.982	4.78	51.3	9.36	42.8	419
BP9	56.78	166.22	178.24	1.01	5.34	63.8	9.11	43.8	424
BP10	76.69	154.579	163.045	0.819	4.17	47.9	11.3	51.6	478
BP11	98.88	155.037	155.438	0.422	2.08	23.0	12.5	55.3	484
BP12	58.31	171.148	172.96	0.937	5.13	63.7	9.66	45.5	448
BP13	99.65	138.484	181.321	0.888	3.78	33.4	7.87	37.3	373
BP14	71.03	165.604	175.971	0.875	4.63	55.0	9.36	44.9	418
BP15	71.03	217.656	218.738	0.788	4.84	67.7	5.12	27.7	298
BP16	71.33	203.796	229.092	0.895	5.15	66.0	4.49	25.0	280
BP18	147	194.647	197.403	0.240	1.30	15.9	5.57	26.8	258
BP19	165.8	190.082	195.999	0.133	0.646	6.67	5.50	26.0	246
BP20	191.8	198.376	199.721	0.0653	0.284	2.32	5.05	23.9	223
BP21	57.475	288.031	299.536	0.756	5.29	85.5	2.37	15.2	231
BP22	71.42	247.224	258.382	0.777	5.04	74.3	3.31	18.8	248
BP23	62.69	162.397	190.822	1.06	5.42	61.5	7.21	35.7	372

Table 10. Production cross sections for HPs from Table 2 in fb for X + dijet at proton-proton colliders for varying center-of-mass energies. No VBF cuts were applied.

No.	M_H	M_A	$M_{H^\pm}$	$(AA)_{13}$	$(AA)_{27}$	$(AA)_{100}$	$(H^+H^-)_{13}$	$(H^+H^-)_{27}$	$(H^+H^-)_{100}$
HP1	176	291.36	311.96	0.319	2.20	34.4	1.47	9.57	136
HP2	557	562.316	565.417	0.00145	0.0112	0.143	0.0769	0.674	10.2
HP3	560	616.32	633.48	0.0107	0.126	3.12	0.0643	0.718	15.8
HP4	571	676.534	682.54	0.0169	0.234	6.90	0.0587	0.751	19.9
HP5	671	688.108	688.437	-	0.0105	0.239	0.0295	0.320	5.71
HP6	713	716.444	723.045	-	0.00762	0.149	0.0230	0.266	4.99
HP7	807	813.369	818.001	-	0.00553	0.137	0.0117	0.160	3.37
HP8	933	939.968	943.787	-	0.00165	0.0340	0.00492	0.0821	1.94
HP9	935	986.22	987.975	-	0.0162	0.696	0.00482	0.0945	3.00
HP10	990	992.36	998.12	-	0.00131	0.0275	0.00349	0.0640	1.61
HP11	250.5	265.49	287.226	0.0423	0.200	1.64	1.39	7.76	84.4
HP12	286.05	294.617	332.457	0.175	0.772	5.89	0.853	5.29	66.0
HP13	336	353.264	360.568	0.0136	0.0829	1.00	0.565	3.56	42.1
HP14	326.55	331.938	381.773	0.216	0.959	7.00	0.499	3.38	45.7
HP15	357.6	399.998	402.568	0.0200	0.157	2.77	0.375	2.57	34.0
HP16	387.75	406.118	413.464	0.00768	0.0498	0.622	0.318	2.18	28.0
HP17	430.95	433.226	440.624	0.00490	0.0316	0.361	0.240	1.72	22.5
HP18	428.25	453.979	459.696	0.00640	0.0486	0.756	0.203	1.52	20.8
HP19	467.85	488.604	492.329	0.00396	0.0311	0.484	0.148	1.17	16.4
HP20	505.2	516.58	543.794	0.00550	0.0388	0.397	0.0982	0.852	13.3

Note that we did not apply VBF-like cuts, as, depending on the parameter point, different channels contribute; for AA production, this can for example, be gluon-gluon or vector-boson fusion to h with successive decays to AA, as well as diagrams with for example, a charged scalar in the t-channel. For H^+H^- final states, standard dijet production with Z/γ radiation with successive decay into H^+H^- can also play a significant role.

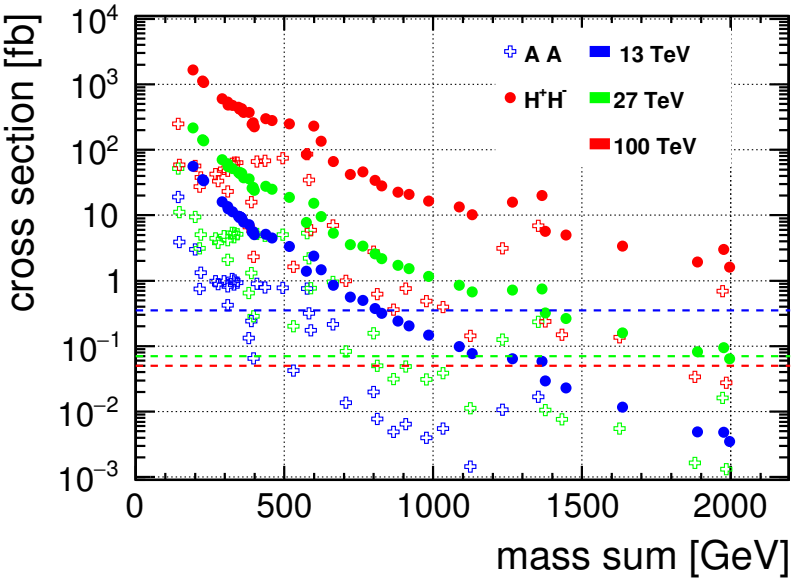

Figure 6. Production cross sections for benchmarks from Tables 1 and 2 as a function of the produced scalar mass sum, for VBF production channels, for 13 TeV, 27 TeV and 100 TeV proton collider options. Horizontal dashed lines indicate minimal cross sections required to produce 1000 events at the respective energy, assuming design luminosity.

For AA production, comparing to non-VBF like topologies, we encounter enhancement rates up to three orders of magnitude when considering the VBF-like contribution, especially for example, for HP14 and HP20, where the largest relative growth takes place for 13 TeV. However, at this center-of-mass energy the total rate remains small. If we consider accessible points only, with at least 1000 events being produced over the full run in the VBF mode, the largest enhancement can be seen for HP20 at 100 TeV and HP14 at 27 TeV or 100 TeV, where the production cross section increases by roughly three orders of magnitude. A detailed analysis for the latter point shows that the predominant contribution for this point at, for example, 100 TeV stems from off-shell H^+A production and subsequent decay $H^+ \to W^+A$ as well as processes decribed by diagrams with a charged scalar in the t-channel, initiated by WW fusion. Note this identification stems from graph identification within Madgraph5; in general, only the complete set of WW initiated diagrams is gauge-invariant. The above statement has been derived by evaluations in the unitary gauge.

Enhancements by more than an order of magnitude are also observed for HPs 11 and 12 at the same center-of-mass energies 27 TeV and 100 TeV, HPs 2 and 16 at 100 TeV, followed by BP 2 accessible already in Run II and BP 20 at 100 TeV. At 13 TeV, the cross section for BP 2 rises from $\sim$ 1.5 fb to $\sim$ 19 fb when VBF-like topologies are considered. This can again be traced back mainly to contributions from $H^\pm A$ production with successive decays $H^\pm \to A\,W^\pm$. At 13 TeV, for example, BPs 11 and 13 might now be accessible at the HL-LHC in the AA VBF channel. At 27 TeV, BP20 as well as 7 additional HPs might now be visible; at 100 TeV, nearly all HPs have large enough cross sections in this channel, with only HPs 8 and 10 having cross sections $\lesssim$ 0.04 fb. We show the enhancement for points with more than 1000 events with full integrated luminosity in Figure 7.

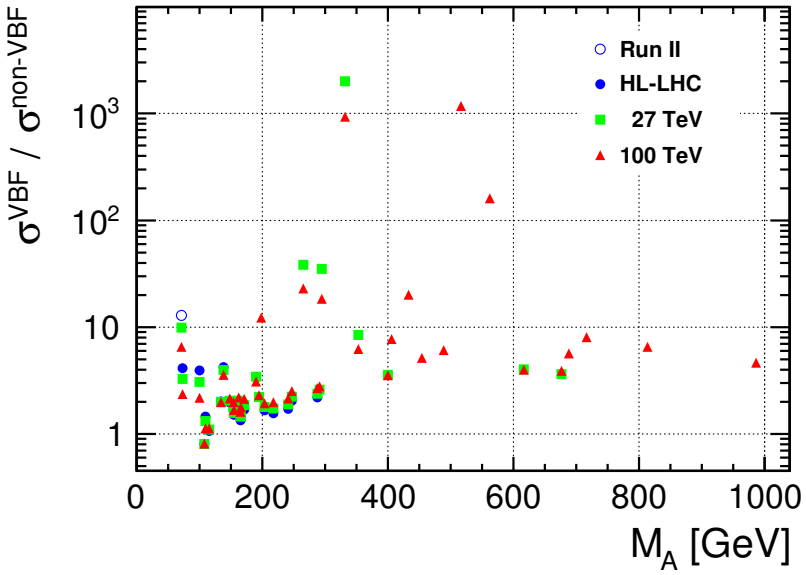

Figure 7. Enhancement of AA production cross sections at pp colliders with various center-of-mass energies when VBF-type topologies are included. Only points with minimal cross-section requirements as specified in the text are shown. See detailed discussion in main body of paper.

In Figure 6, although in general a decrease in the cross sections is observed for rising masses, there are points which deviate from this behaviour, as, for example, the production cross sections for $AAjj$ at 100 TeV. As an example, HP4 here leads to a cross section of about 7 fb , while the production cross section for HP5 is more an order of magnitude lower, while masses of A are quite similar. This can be traced back to the production of an off-shell h with two jets, where the h subsequently decays to AA. This process is mediated via the $\bar{\lambda}_{345}$ coupling, which grows with the difference between M_H^2 and M_A^2. In fact, concentrating on the dominant contribution, namely $gg \to h^* g g$, with subsequent decays $h^* \to A A$, we find that $\left(\frac{\bar{\lambda}_{345,HP5}}{\bar{\lambda}_{345,HP4}}\right)^2 \sim 0.026$. The production cross sections in this mode are 4.7 fb and 0.11 fb for HP4 and HP5, respectively, displaying the same ratio. Additional contributions in both points stem from VBF diagrams with, for example, a charged or neutral scalar in the t-channel; for HP 4/ 5, these contribute roughly 4% /10% to the total cross section.

For the $H^+ H^-$ channel, the VBF-induced cross sections are up to a factor of 2 larger than for the direct production; maximal enhancement is observed for HP4 at 100 TeV. In fact, enhancements can mainly present for this collider option. In contrast, for example, for BP3 at 13 TeV, the VBF-type cross section only amounts to about 20% of the direct production. As before, we note a general decrease of the cross sections as masses rise. However, we can again observe that for similar mass scales, there can be exceptions where cross sections differ by about a factor 3. Again, this can be traced back to diagrams that are mediated via the SM-like scalar h. The coupling between h and H^+H^- is given by

$$\lambda_3 \equiv \lambda_{345} - 2\frac{M_H^2 - M_{H^\pm}^2}{v^2}.$$

As an example, we can consider production cross sections for BP21 and HP11 at 100 TeV; both points feature similar charged scalar masses, however, the mass differences to the dark matter candidate vary largely. For BP21, we have $\lambda_3 \sim 2.9$, while for HP11, the corresponding value is given by $\lambda_3 \sim 0.5$. This leads to a relative factor of around 30 for contributions which are triggered by h-exchange in the s-channel. In fact, the corresponding cross sections stemming from gluon-fusion are 118 fb for BP21 and 4 fb for HP11, reflecting this ratio. Other diagrams come from $p\,p \to j\,j\,\gamma\,(Z)$, with the electroweak gauge boson decaying into the charged scalars, as well as diagrams with charged scalars

in the t-channel. Due to quantum interference, it is not obvious to disentangle these from h-induced contributions. However, for HP11 it can be stated that gg-induced processes contribute roughly $\sim$ 5% to the total cross section, while the corresponding number for BP21 is $\gtrsim$ 50%. Similarly, one can compare cross sections for HP4 and HP5 a 100 TeV center-of-mass energy; although these points feature similar charged scalar masses, the cross sections differ by a factor 3.5. This can again be traced back to differences in λ_3, which is given by 4.15/0.64 for HP4/HP5, respectively. Comparing numbers from gg-induced processes only, which are dominantly mediated via h-exchange, we find that the cross sections are given by 10.5 fb and 0.229 fb respectively, representing the above hierarchy in the coupling. In other channels, processes which are h-mediated are contributing mainly for HP4. As before, a clear disentanglement is not possible due to interference effects, however, one can state that for HP4 at least 50% of the total cross section are mediated via h, while this number goes down to about 4% for HP5.

In summary, for AA final states inclusion of processes with additional jets can greatly improve the collider reach. For $H^+ H^-$, instead, maximal enhancements reach a factor 2 at a 100 TeV collider, while for lower center-of-mass energies the respective cross sections can be up to a factor 5 smaller than the direct production channel.

5.6. Purely Photon-Induced Processes

We also briefly comment on the possibility of observing photon-induced production processes using forward proton spectrometers, as for example, discussed in [98–100]. Here, photons are emitted from the protons, and the final state $p' p' + X$ is measured, with X being the final state generated via photon-fusion and p' denoting intact protons in the final state, which could be measured in the proton spectrometers. For the IDM, the only possible process into novel final states is given by

$$p\,p \;\to\; p'\,p'\,H^+\,H^-,$$

as no other BSM final state can be generated via photon-photon fusion at tree-level. In principle processes would be possible via the photon-photon-Higgs vertex, possibly allowing for AA photo-production, and also contribute to the above process, albeit at higher order. This is currently not implemented in our framework and beyond the scope of the current work. We present the production cross-sections for all benchmark scenarios in Tables 11 and 12, respectively.

Table 11. Production cross sections for BPs from Table 1 in fb for $Xp'p'$ at a 13 and 100 TeV pp collider. No cuts are applied on the scattered proton kinematics.

No.	M_H	M_A	$M_{H^\pm}$	$(H^+H^-)_{13}$	$(H^+H^-)_{100}$
BP1	72.77	107.803	114.639	0.404	2.63
BP2	65	71.525	112.85	0.425	2.74
BP3	67.07	73.222	96.73	0.695	4.14
BP4	73.68	100.112	145.728	0.184	1.37
BP6	72.14	109.548	154.761	0.150	1.16
BP7	76.55	134.563	174.367	0.100	0.833
BP8	70.91	148.664	175.89	0.0971	0.817
BP9	56.78	166.22	178.24	0.0927	0.786
BP10	76.69	154.579	163.045	0.126	1.00
BP11	98.88	155.037	155.438	0.148	1.15
BP12	58.31	171.148	172.96	0.103	0.855
BP13	99.65	138.484	181.321	0.0875	0.750
BP14	71.03	165.604	175.971	0.0970	0.814
BP15	71.03	217.656	218.738	0.0455	0.440
BP16	71.33	203.796	229.092	0.0384	0.388
BP18	147	194.647	197.403	0.0651	0.592
BP19	165.8	190.082	195.999	0.0667	0.604
BP20	191.8	198.376	199.721	0.0625	0.572
BP21	57.475	288.031	299.536	0.0143	0.181
BP22	71.42	247.224	258.382	0.0248	0.277
BP23	62.69	162.397	190.822	0.0734	0.651

Table 12. Production cross sections for HPs from Table 2 in fb for $Xp'p'$ at a 13 and 100 TeV pp collider. No cuts are applied on the scattered proton kinematics.

No.	M_H	M_A	$M_{H^\pm}$	$(H^+H^-)_{13}$	$(H^+H^-)_{100}$
HP1	176	291.36	311.96	0.0122	0.161
HP2	557	562.316	565.417	0.00106	0.0276
HP3	560	616.32	633.48	-	0.0194
HP4	571	676.534	682.54	-	0.0154
HP5	671	688.108	688.437	-	0.0150
HP6	713	716.444	723.045	-	0.0128
HP7	807	813.369	818.001	-	0.00868
HP8	933	939.968	943.787	-	0.00547
HP9	935	986.22	987.975	-	0.00471
HP10	990	992.36	998.12	-	0.00457
HP11	250.5	265.49	287.226	0.0167	0.205
HP12	286.05	294.617	332.457	0.00958	0.134
HP13	336	353.264	360.568	0.00699	0.106
HP14	326.55	331.938	381.773	0.00557	0.0895
HP15	357.6	399.998	402.568	0.00450	0.0766
HP16	387.75	406.118	413.464	0.00403	0.0709
HP17	430.95	433.226	440.624	0.00310	0.0587
HP18	428.25	453.979	459.696	0.00261	0.0514
HP19	467.85	488.604	492.329	0.00195	0.0420
HP20	505.2	516.58	543.794	0.00127	0.0310

No cuts on the scattered proton kinematics are applied. As for direct pair-production, the cross sections are determined by the available phase space, given by the masses of the charged scalars, and exhibit decline with rising mass scales. The production cross sections are lower by factors 300 for 13 TeV and up to 800 for 100 TeV with respect to the direct pair-production cross sections, given in Tables 3, 4 and 7, 8 for 13 TeV and 100 TeV, respectively. Therefore, all points here would in principle be within reach first in direct pair-production, using again our simple counting criterium. The photon-fusion mode would in principle provide an additional test of the model for photon induced processes. However, even not taking into account the acceptance of the proton spectrometers only BPs 1-3 would be accessible at the HL-LHC, corresponding to a mass range up to 200 GeVfor the sum of the produced particles. At 100 TeV, all low mass points as well as HPs 1, 11-18 would be accessible, enhancing the mass range to 900 GeV.

5.7. Muon Collider

Recently, discussions of a muon collider have again raised some interest in the community (see e.g., [101]). We therefore present cross sections at such a collider for two collider options, namely, for center-of-mass energies of 10 TeV and 30 TeV. Note that without taking beamstrahlung and initial state radiation effects into account, the cross sections for $\mu^+\mu^-$ and e^+e^- induced processes are the same as lepton masses are negligible for the considered center-of-mass energies. Since beamstrahlung and initial state radiation effects are much less important for $\mu^+\mu^-$ they were therefore not taken into account in the presented study.

For direct production, we found that cross sections are similar for all BPs and HPs, given by 0.13 fb for HA production and 0.31 fb for H^+H^- production at the 10 TeV collider, respectively; cross sections at 30 TeV are about an order of magnitude lower. Cross sections might slightly rise due to radiative return (see e.g., [102]). We therefore list results for VBF-type production modes only; in particular, we consider

$$\mu^+\mu^- \to \nu_\mu \bar{\nu}_\mu AA, \quad \mu^+\mu^- \to \nu_\mu \bar{\nu}_\mu H^+H^-.$$

Production cross sections for these processes can be found in Tables 13 and 14, and are compared in Figure 8.

Depending on the parameter point, different diagrams contribute. For the low-mass BPs, production cross sections range between 0.06 fb and 1.17 fb at 10 TeV and between 0.1 fb and 3 fb at 30 TeV. For example, the dominant contribution to the cross section for AA final states at BP21, the benchmark point with the highest rates, stems from diagrams with a charged scalar in the t-channel. For high-mass HPs, cross sections start basically an order of magnitude lower, and can reach up to roughly 1 fb at both center-of-mass

energies, depending on the benchmark point and production mode. Note that for H^+H^- the VBF-like production almost always renders rates higher than direct pair-production, with the exception of the HPs at 10 TeV center-of-mass energy. For example, for BP3 at 30 TeV, diagrams with W-boson fusion to a Z-boson or photon with successive decay to $H^+ H^-$ are predominant, with slightly lower contributions from diagrams with an A or H in the t-channel.

Table 13. Production cross sections for BPs from Table 1 in fb for $X\nu_\mu\bar{\nu}_\mu$ at a 10 and 30 TeV muon-collider.

No.	M_H	M_A	$M_{H^\pm}$	$(AA)_{10}$	$(H^+H^-)_{10}$	$(AA)_{30}$	$(H^+H^-)_{30}$
BP1	72.77	107.803	114.639	0.476	0.828	0.732	1.03
BP2	65	71.525	112.85	0.678	0.714	1.00	1.09
BP3	67.07	73.222	96.73	0.426	0.825	0.641	1.22
BP4	73.68	100.112	145.728	0.798	0.549	1.22	0.946
BP6	72.14	109.548	154.761	0.954	0.551	1.47	0.834
BP7	76.55	134.563	174.367	0.787	0.451	1.24	0.767
BP8	70.91	148.664	175.89	0.714	0.463	1.15	0.807
BP9	56.78	166.22	178.24	0.813	0.600	1.33	0.921
BP10	76.69	154.579	163.045	0.521	0.515	0.837	0.857
BP11	98.88	155.037	155.438	0.286	0.452	0.464	0.698
BP12	58.31	171.148	172.96	0.600	0.564	0.984	0.969
BP13	99.65	138.484	181.321	0.567	0.366	0.904	0.680
BP14	71.03	165.604	175.971	0.754	0.601	1.23	0.860
BP15	71.03	217.656	218.738	0.880	0.610	1.51	0.919
BP16	71.33	203.796	229.092	1.17	0.519	1.98	0.817
BP18	147	194.647	197.403	0.214	0.296	0.362	0.515
BP19	165.8	190.082	195.999	0.121	0.247	0.209	0.442
BP20	191.8	198.376	199.721	0.0586	0.210	0.106	0.385
BP21	57.475	288.031	299.536	1.45	0.595	2.67	1.14
BP22	71.42	247.224	258.382	1.05	0.504	1.85	0.931
BP23	62.69	162.397	190.822	1.41	0.478	2.13	0.832

Table 14. Production cross sections for HPs from Table 2 in fb for $X\nu_\mu\bar{\nu}_\mu$ at a 10 and 30 TeV muon-collider.

No.	M_H	M_A	$M_{H^\pm}$	$(AA)_{10}$	$(H^+H^-)_{10}$	$(AA)_{30}$	$(H^+H^-)_{30}$
HP1	176	291.36	311.96	0.691	0.240	1.28	0.470
HP2	557	562.316	565.417	0.00892	0.0265	0.0211	0.0639
HP3	560	616.32	633.48	0.143	0.0506	0.356	0.128
HP4	571	676.534	682.54	0.229	0.0777	0.602	0.206
HP5	671	688.108	688.437	0.0103	0.0184	0.0268	0.0473
HP6	713	716.444	723.045	0.0110	0.0181	0.0295	0.0474
HP7	807	813.369	818.001	0.00910	0.0144	0.0263	0.0397
HP8	933	939.968	943.787	0.00324	0.00792	0.00986	0.0226
HP9	935	986.22	987.975	0.0297	0.0144	0.103	0.0460
HP10	990	992.36	998.12	0.00312	0.00695	0.00991	0.0201
HP11	250.5	265.49	287.226	0.0760	0.116	0.141	0.230
HP12	286.05	294.617	332.457	0.170	0.0996	0.320	0.204
HP13	336	353.264	360.568	0.0392	0.0722	0.0785	0.152
HP14	326.55	331.938	381.773	0.151	0.0746	0.295	0.159
HP15	357.6	399.998	402.568	0.0677	0.0678	0.139	0.145
HP16	387.75	406.118	413.464	0.0291	0.0533	0.0609	0.117
HP17	430.95	433.226	440.624	0.0203	0.0473	0.0438	0.105
HP18	428.25	453.979	459.696	0.0308	0.0435	0.0669	0.0979
HP19	467.85	488.604	492.329	0.0208	0.0368	0.0464	0.0849
HP20	505.2	516.58	543.794	0.0359	0.0326	0.0824	0.0773

As before, in general, one can observe a decrease of production cross sections with rising mass scales, where however some exceptions exist. For H^+H^- production, it is again instructive to compare cross sections for BP21 and HP11, which feature similar charged scalar masses but different M_H, leading to a factor 5 difference in production cross sections at 30 TeV. This difference can be traced back to the interference between two different gauge-invariant sets of diagrams which contribute to this process, with W^+W^- and $W\mu$ fusion, which we label GI I and GI II, respectively; the two sets of diagrams are displayed in Appendix B. Contributions from these sets of diagrams are shown in Table 15 where we also consider two additional parameter points HP11b and HP11c, which have the same charged or charged and dark matter mass as BP21. We see that, while contributions to GI II mainly depend on the masses of the charged scalars, in GI I the masses of the neutral dark scalars also play a role via diagrams with these particles in the t-channel.

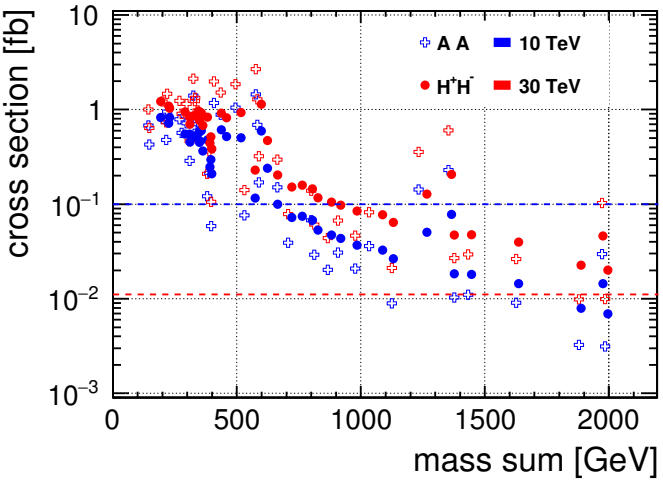

Figure 8. Production cross sections for benchmarks from Tables 1 and 2 as a function of the produced scalar mass sum, for AA and H^+H^- production at 10 TeV and 30 TeV muon collider. Horizontal dashed lines indicate minimal cross sections required to produce 1000 events at the respective energy, assuming 5 year integrated design luminosity.

Table 15. Transition between BP21 and HP11, including different contributions from gauge-invariant sets of diagrams with WW (GI I) and $W\mu$ (GI II) fusion, for H^+H^- production in the VBF-like mode at a muon collider with 30 TeV center-of-mass energy. Masses are in GeV and cross sections in fb. See text for details.

	BP21	**HP11**	**HP11b**	**HP11c**
M_{H^+}	299.536	287.226	299.536	299.536
M_H	57.475	250.5	250.5	57.475
M_A	288.031	265.49	265.49	265.49
GI I	19.01(7)	19.69(8)	18.04(6)	18.76(7)
GI II	17.89(5)	19.43(5)	17.83(5)	17.86(6)
Equation (14)	1.12 (9)	0.23(9)	0.21(7)	0.90(9)
GI I + GI II	1.129(3)	0.2293(6)	0.2274(7)	0.973(3)
total	1.144(5)	0.2297(7)	0.2276(8)	0.968(3)

From the table, we observe that the final contribution seems to dominantly stem from a fine-tuned cancellation between these two type of diagrams according to

$$\int_{PS} |\mathcal{M}_I + \mathcal{M}_{II}|^2 \simeq \int_{PS} \left(|\mathcal{M}_I|^2 - |\mathcal{M}_{II}|^2 \right), \tag{14}$$

where $\mathcal{M}_i = |\mathcal{M}_i| e^{i\varphi_i}$ and $\int_{PS}$ denotes integration over phase space. The above equation is, for example, fulfilled if the integrated matrix elements differ by a phase and obey

$$\int_{PS} |\mathcal{M}_{II}|^2 \simeq -\int_{PS} |\mathcal{M}_I||\mathcal{M}_{II}| \cos(\varphi_{II} - \varphi_I).$$

A similar observation can be made by comparing HP4 and HP5, which feature similar scalar masses but vary in the mass differences between M_{H^+} and M_H. A detailed study shows that, as before, a larger mass gap increases contributions from GI I, therefore leading to a larger total result.

For the AA channel, things are slightly different. Here, the main contribution stems from WW fusion only, where the corresponding diagrams can be found in Appendix C. It is instructive to consider the contributions triggered by h- exchange, with the coupling strength $\bar{\lambda}_{345}$ (cf. Equation (13)), with respect to the remaining diagrams. Note that this discussion now assumes unitary gauge; in general, the above split is not gauge-invariant. We again consider HP4 and HP5 at 30 TeV; these points have similar charged and heavier

neutral scalar masses, but largely different M_H, resulting in different $\bar{\lambda}_{345}$ values. We list the separate contributions in Table 16. Note that the total contribution is dominated by the $h-$exchange diagram for HP4, corresponding to the relatively large $\bar{\lambda}_{345}$ value. From the table, we can see that indeed the different terms are found to be proportional to the ratio of the hH^+H^- coupling squared.

Table 16. Comparison of different contributions to AA final state in the VBF-like production mode at a muon collider with the center-of-mass energy of 30 TeV. Masses are given in GeVand cross sections in fb.

	HP4	**HP5**
M_A	676.534	688.108
M_{H^+}	682.54	688.437
M_H	571	671
$\bar{\lambda}_{345}$	3.88	0.62
h-exchange only	0.510(2)	0.01259(4)
all others	0.01625(4)	0.01347(5)
interference	0.078(4)	0.0008(1)
total	0.604(3)	0.02686(9)

In general, however, the total contribution depends on all three dark scalar masses. This can be seen in Table 17, where we compare BP21, HP12, as well as variations around BP21 where we vary the mass differences between the dark scalars. Comparing BP21b and BPP21c, we observe that the contribution from h-exchange is directly proportional to $\bar{\lambda}^2_{345}$, as expected. For a similar mass range of M_A, we can therefore tune the total cross section by at least an order of magnitude by varying the other dark scalar masses.

Table 17. Comparison of different contributions to AA final state in the VBF-like production mode at a muon collider with the center-of-mass energy of 30 TeV. Masses are given in GeV and cross sections in fb.

	BP21	**HP12**	**BP21b**	**BP21c**
M_A	288.031	294.617	288.031	288.031
M_{H^+}	299.536	332.457	329.536	329.536
M_H	57.475	286.05	57.475	280.031
$\bar{\lambda}_{345}$	2.63	0.277	2.63	0.152
h-exchange only	2.25(1)	0.2155(8)	2.067(8)	0.00689(3)
all others	0.00706(2)	0.1899(5)	0.2223(7)	0.2216(8)
interference	0.36(1)	0.1094(9)	1.19(1)	0.067(1)
total	2.68(1)	0.3208(8)	3.48(1)	0.295(1)

In [103], the authors give a rough estimate of integrated luminosity that could be achieved at a muon collider, as a function of the center-of-mass energy. In particular

$$\int \mathcal{L} \sim \left(\frac{\sqrt{s}}{10\,\text{TeV}}\right)^2.$$

For a 10 TeV collider, they estimate an integrated luminosity of $10\,\text{ab}^{-1}$ for a 5-year run. Applying the above expression for the higher center-of-mass energy, we roughly expect the integrated luminosity to be larger by one order of magnitude.

The authors equally state that target processes at 10 TeV should have cross sections of $\mathcal{O}(\text{fb})$, with a similar rescaling at 30 TeV. Using this criterium, we see that at 10 TeV only BPs 16, 21, 22, and 23 would be accessible in the VBF-like production of AA, while none of the HPs can be tested. At 30 TeV, all low mass BPs are accessible; in the high mass region, HPs 2, 5-8, 10 and 18-20 render too low cross sections. This corresponds to a maximal mass range of about $\sum_i M_i = 1400\,\text{GeV}$.

In accordance with the previous discussion, we can again alternatively require that at least 1000 events are produced in order to assess accessibility of a certain benchmark point. Using this criterium, all low mass BPs would be accessible during a 5 year run

at 10 TeV in all channels, with the exception of AA production for BP20; this channel however provides a large enough cross section at 30 TeV. For the high-mass HPs, HPs 1, 3, 4, 12 and 14 would be accessible in the AA channel, where HP 1 and 11 have large enough cross sections in the H^+H^- channel. This corresponds to a mass range of up to 600 GeV(1400 GeV) in the H^+H^- (AA) channel. At 30 TeV, all HPs would be accessible.

We want to emphasize again that the accessibility criterium of 1000 generated events can only be regarded as a first approximation and was introduced for comparison only; obviously, detailed investigations are needed in order to determine the true discovery range. We however consider this an easy selection criterium. More detailed results for investigation and reachability of the discussed benchmarks scenarios at CLIC can be found for example, in [33,51,104].

6. Conclusions

We have presented several benchmarks for the Inert Doublet Model, a Two Higgs Doublet Model with a dark matter candidate, and provided predictions for the pair-production of dark scalars at the 13 TeV LHC, a high-energy upgrade, as well as a possible 100 TeV proton-proton collider. We also gave predictions for pair-production cross sections at possible $\mu^+\mu^-$ colliders with various center-of-mass energies. Applying a simple counting criterium, we categorize these benchmarks in terms of their possible accessibility at different facilities. For example, after the high-luminosity run of the LHC, assuming target luminosity, for the low BPs in table 1 all channels should be accessible, apart from the AA final state which is suppressed due to small absolute values of the coupling λ_{345}. Taking additionally VBF-like topologies into account for this final state then renders all but BPs 18 - 20 accessible after the HL-LHC run. For the high benchmark points HPs 1 and 11-17 should be accessible in all but the AA channel; for HPs 18 and 19, in addition the $A\,H^-$, $H\,H^-$ production modes render lower cross sections. For HP20, only the HH^+ and AH^+ channels look feasible. This corresponds to a possible reach up to about 500 GeV for scalar masses. For AA, masses up to 300 GeV render large enough cross sections. We also briefly comment on the possibility of using proton spectrometers at hadron colliders to tag processes induced via photon-photon fusion. At tree-level, only charged scalar pair-production is possible. Cross sections for these processes are much smaller than for direct pair-production, but some points are within range at both HL-LHC as well as a 100 TeV collider assuming high tagging efficiency of forward proton spectrometers.

In turn, several possible future scenarios are considered: a high-energy upgrade to a center of mass energy of 27 TeV, a 100 TeV proton-proton facility, as well as a possible muon collider with different energy stages. For CLIC, detailed studies are available and have been presented in [33,51,104–106]; we therefore omit their discussion here. The main result for 3 TeV CLIC is that the discovery reach for charged scalar pair-production extends to up to scalar masses of 1 TeV. At 27 TeV, we find that the range up to 1 TeV can basically be covered in all channels, although some of the BPs and HPs still remain elusive in the AA channel. At a 100 TeV collider, the number of HPs that remain inaccessible in this channel decreases. Including again AA production with additional jets, only two of the HP points remain inaccessible in this channel according to our simple counting criterium.

At a muon collider, we can again discuss both direct as well as VBF-like production channels. For direct production, AH as well as H^+H^- seem to be accessible at all center-of-mass energies considered for all BPs and HPs. For the VBF-like probes, with 10 TeV center-of-mass energy, basically all low-mass BPs as well a subset of high-mass HPs are accessible for AA production, which might provide an interesting cross check. This corresponds to a mass scale for M_A in this channel of about 700 GeV. At 30 TeV, all channels should be accessible assuming target luminosity over the whole runtime. In addition, for almost all scenarios the VBF-induced production of H^+H^- gives higher cross sections than direct pair-production, with the exception of the HPs at 10 TeV.

We again want to emphasize that our rough criterium needs to be supported by detailed studies for each scenario, including both signal and background. However, we

consider the BPs and HPs presented here give useful guidelines for either phenomenological studies or experimental searches.

Author Contributions: Conceptualization, J.K., T.R., D.S., and A.F.Ż.; methodology, T.R. and D.S.; software, T.R. and D.S.; validation, T.R.; formal analysis, T.R.; investigation, T.R.; resources, J.K., T.R., and A.F.Ż.; data curation, T.R.; writing—original draft preparation, T.R. and D.S.; writing—review and editing, J.K., T.R., and A.F.Ż.; visualization, T.R. and A.F.Ż.; supervision, T.R.; project administration, T.R..; funding acquisition, J.K., T.R. and A.F.Ż. All authors have read and agreed to the published version of the manuscript.

Funding: This research was supported in parts by the National Science Centre, Poland, the HARMONIA project under contract UMO-2015/18/M/ST2/00518 (2016–2021) and OPUS project under contract UMO-2017/25/B/ST2/00496 (2018–2021). It is also partially based upon work from COST Action CA16201 PARTICLEFACE, supported by COST (European Cooperation in Science and Technology, www.cost.eu). The work of TR was partially supported by grant K 125105 of the National Research, Development and Innovation Fund in Hungary.

Data Availability Statement: The data presented in this study are available on request from the corresponding author.

Acknowledgments: JK thanks Gudrid Moortgat-Pick for her hospitality and the DFG for support through the SFB 676 "Particles, Strings and the Early Universe" during the initial stage of this project. We also want to thank the `MicrOMEGAs` authors for useful discussions regarding different versions of their code.

Conflicts of Interest: The authors declare no conflict of interest.

Appendix A. Benchmark Tables Using `micrOMEGAs_5.2.4`

We present the benchmark points from Table 1, were `micrOMEGAs_5.2.4` has been used in the relic density calculation, in Table A1. For selected benchmark points, deviations can be up to 7%. We also present values for `micrOMEGAs_5.0.4` for `fast=0` in the integration setup (see [89] for details).

Table A1. As Table 1 (without λ_2 and on or offshell information for intermediate gauge bosons), with dark matter relic density calculated using `micrOMEGAs_5.2.4` and `micrOMEGAs_5.0.4` with `fast=0`. Note that several benchmark points, selected previously to match PLANCK measurements, result in relic density slightly above the assumed limit (indicated by slashed font).

No.	M_H	M_A	$M_{H^\pm}$	λ_{345}	$\Omega_H h^2$ `5.0.4`	$\Omega_H h^2$ `5.2.4`	$\Omega_H h^2$ `5.0.4, fast=0`
BP1	72.77	107.803	114.639	−0.00440723	0.11998	0.12277	0.12245
BP2	65	71.525	112.85	0.0004	0.07076	0.07085	0.070725
BP3	67.07	73.222	96.73	0.00738	0.06159	0.061706	0.061569
BP4	73.68	100.112	145.728	−0.00440723	0.089114	0.08854	0.088507
BP6	72.14	109.548	154.761	−0.00234	0.117	0.12155	0.12104
BP7	76.55	134.563	174.367	0.0044	0.031381	0.031334	0.031303
BP8	70.91	148.664	175.89	0.0058	0.12207	0.122618	0.12537
BP9	56.78	166.22	178.24	0.00338	0.081243	0.081226	0.080547
BP23	62.69	162.397	190.822	0.0056	0.065	0.0608	0.062146
BP10	76.69	154.579	163.045	0.0096	0.028125	0.028312	0.028293
BP11	98.88	155.037	155.438	−0.0628	0.002735	0.002735	0.0027319
BP12	58.31	171.148	172.96	0.00762	0.0064104	0.0064098	0.0063558
BP13	99.65	138.484	181.321	0.0532	0.0012541	0.0012541	0.0012534
BP14	71.03	165.604	175.971	0.00596	0.11833	0.12245	0.12169
BP15	71.03	217.656	218.738	0.00214	0.12217	0.12647	0.12571
BP16	71.33	203.796	229.092	−0.00122	0.12205	0.12686	0.12615
BP18	147	194.647	197.403	−0.018	0.0017711	0.0017711	0.0017667
BP19	165.8	190.082	195.999	−0.004	0.0028308	0.0028308	0.0028209
BP20	191.8	198.376	199.721	0.008	0.0084219	0.0084219	0.0083755
BP21	57.475	288.031	299.536	0.00192	0.11942	0.11937	0.11845
BP22	71.42	247.224	258.382	−0.0032	0.12206	0.12699	0.1263

Appendix B. Diagrams Contributing to $\mu^+ \mu^- \to H^+ H^- \nu_\mu \bar{\nu}_\mu$

Appendix B.1. Diagrams via W^+W^- Fusion (GI I)

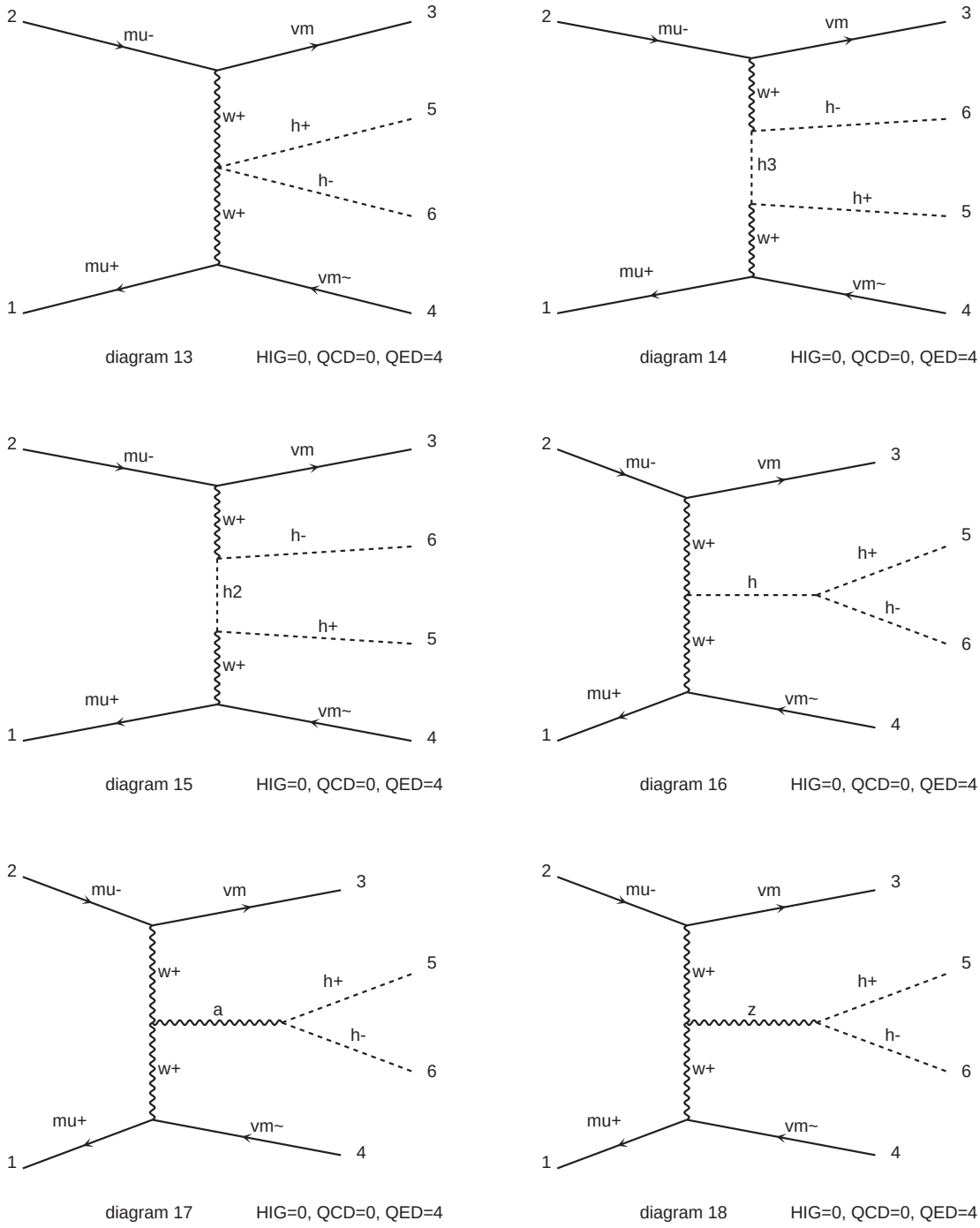

Figure A1. GI I diagrams for W^+W^- fusion.

Appendix B.2. Sample Diagrams via Wμ Fusion (GI II)

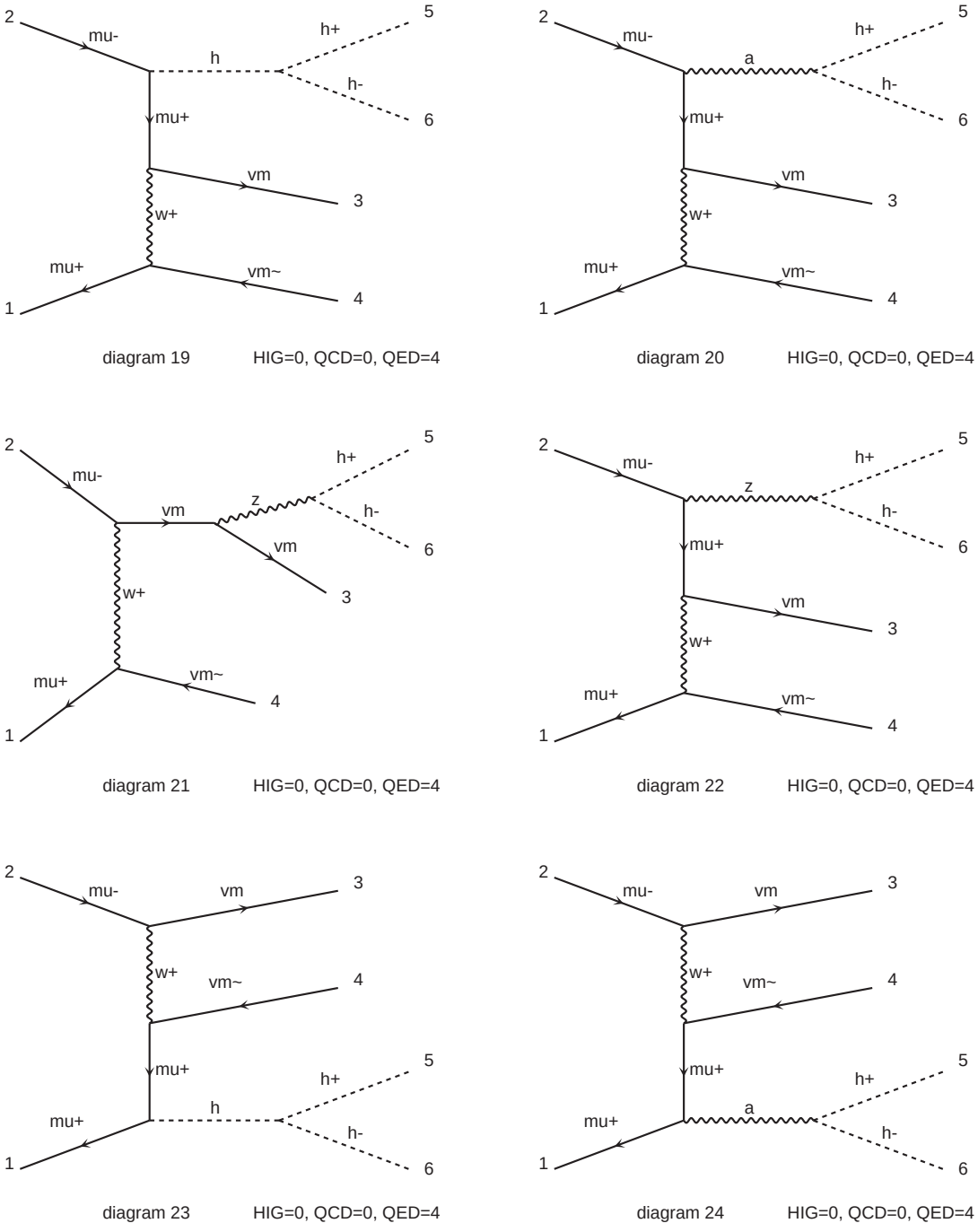

Figure A2. GI II diagrams for $W\mu$ fusion.

Appendix C. Sample Diagrams Contributing to $\mu^+ \mu^- \to A\, A\, \nu_\mu\, \bar{\nu}_\mu$

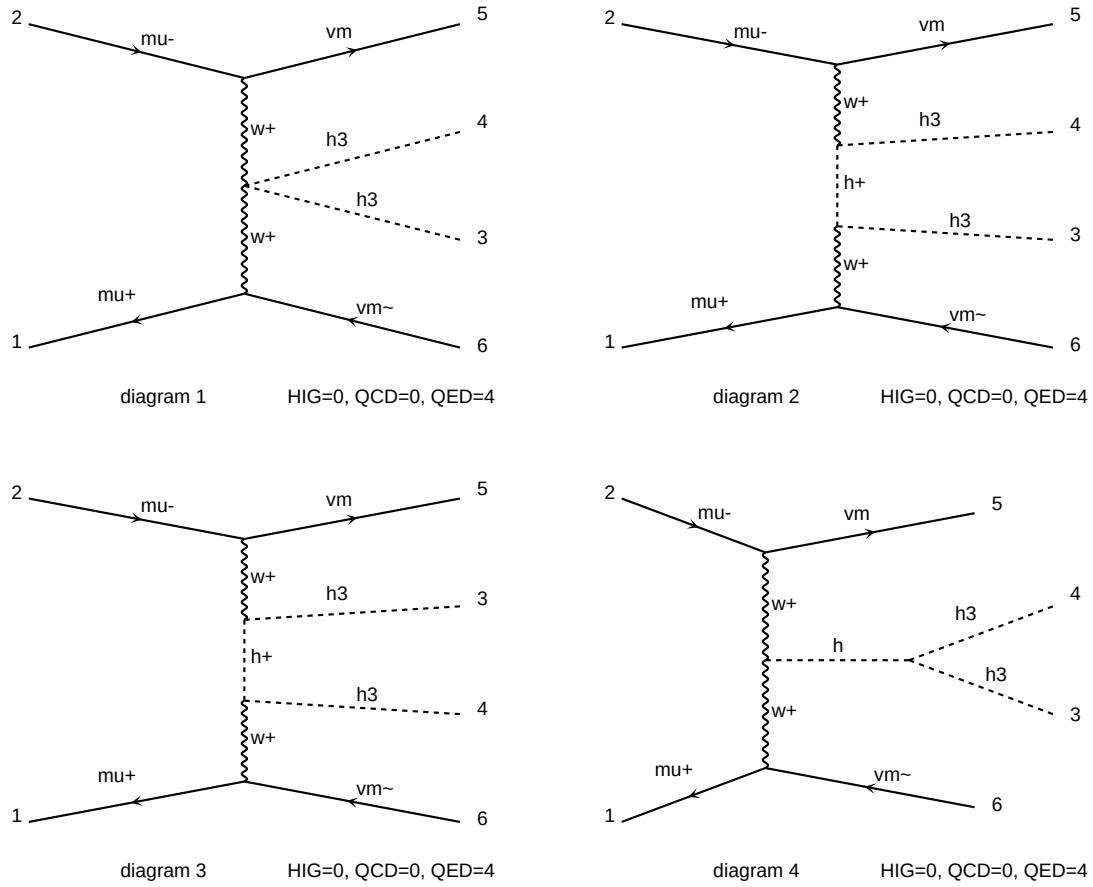

Figure A3. Diagrams for W^+W^- fusion.

References

1. Deshpande, N.G.; Ma, E. Pattern of Symmetry Breaking with Two Higgs Doublets. *Phys. Rev. D* **1978**, *18*, 2574, doi:10.1103/PhysRevD.18.2574.
2. Cao, Q.H.; Ma, E.; Rajasekaran, G. Observing the Dark Scalar Doublet and its Impact on the Standard-Model Higgs Boson at Colliders. *Phys. Rev. D* **2007**, *76*, 095011, doi:10.1103/PhysRevD.76.095011.
3. Barbieri, R.; Hall, L.J.; Rychkov, V.S. Improved naturalness with a heavy Higgs: An Alternative road to LHC physics. *Phys. Rev. D* **2006**, *74*, 015007, doi:10.1103/PhysRevD.74.015007.
4. Lopez Honorez, L.; Nezri, E.; Oliver, J.F.; Tytgat, M.H.G. The Inert Doublet Model: An Archetype for Dark Matter. *J. Cosmol. Astropart. Phys.* **2007**, *0702*, 028, doi:10.1088/1475-7516/2007/02/028.
5. Lopez Honorez, L.; Yaguna, C.E. The inert doublet model of dark matter revisited. *J. High Energy Phys.* **2010**, *09*, 046, doi:10.1007/JHEP09(2010)046.
6. Dolle, E.M.; Su, S. The Inert Dark Matter. *Phys. Rev. D* **2009**, *80*, 055012, doi:10.1103/PhysRevD.80.055012.
7. Goudelis, A.; Herrmann, B.; Stal, O. Dark matter in the Inert Doublet Model after the discovery of a Higgs-like boson at the LHC. *J. High Energy Phys.* **2013**, *09*, 106, doi:10.1007/JHEP09(2013)106.
8. Lundstrom, E.; Gustafsson, M.; Edsjo, J. The Inert Doublet Model and LEP II Limits. *Phys. Rev. D* **2009**, *79*, 035013, doi:10.1103/PhysRevD.79.035013.
9. Dolle, E.; Miao, X.; Su, S.; Thomas, B. Dilepton Signals in the Inert Doublet Model. *Phys. Rev. D* **2010**, *81*, 035003, doi:10.1103/PhysRevD.81.035003.
10. Gustafsson, M.; Rydbeck, S.; Lopez-Honorez, L.; Lundstrom, E. Status of the Inert Doublet Model and the Role of multileptons at the LHC. *Phys. Rev. D* **2012**, *86*, 075019, doi:10.1103/PhysRevD.86.075019.
11. Aoki, M.; Kanemura, S.; Yokoya, H. Reconstruction of Inert Doublet Scalars at the International Linear Collider. *Phys. Lett. B* **2013**, *725*, 302–309, doi:10.1016/j.physletb.2013.07.011.
12. Ho, S.Y.; Tandean, J. Probing Scotogenic Effects in e^+e^- Colliders. *Phys. Rev. D* **2014**, *89*, 114025, doi:10.1103/PhysRevD.89.114025.

13. Arhrib, A.; Tsai, Y.L.S.; Yuan, Q.; Yuan, T.C. An Updated Analysis of Inert Higgs Doublet Model in light of the Recent Results from LUX, PLANCK, AMS-02 and LHC. *J. Cosmol. Astropart. Phys.* **2014**, *1406*, 030, doi:10.1088/1475-7516/2014/06/030.
14. Arhrib, A.; Benbrik, R.; Gaur, N. $H \to \gamma\gamma$ in Inert Higgs Doublet Model. *Phys. Rev. D* **2012**, *85*, 095021, doi:10.1103/PhysRevD.85.095021.
15. Swiezewska, B.; Krawczyk, M. Diphoton rate in the inert doublet model with a 125 GeV Higgs boson. *Phys. Rev. D* **2013**, *88*, 035019, doi:10.1103/PhysRevD.88.035019.
16. Krawczyk, M.; Sokolowska, D.; Swaczyna, P.; Swiezewska, B. Constraining Inert Dark Matter by $R_{\gamma\gamma}$ and WMAP data. *J. High Energy Phys.* **2013**, *09*, 055, doi:10.1007/JHEP09(2013)055.
17. Ginzburg, I.F. Measuring mass and spin of Dark Matter particles with the aid energy spectra of single lepton and dijet at the e^+e^- Linear Collider. *J. Mod. Phys.* **2014**, *5*, 1036–1049, doi:10.4236/jmp.2014.511105.
18. Belanger, G.; Dumont, B.; Goudelis, A.; Herrmann, B.; Kraml, S.; Sengupta, D. Dilepton constraints in the Inert Doublet Model from Run 1 of the LHC. *Phys. Rev. D* **2015**, *91*, 115011, doi:10.1103/PhysRevD.91.115011.
19. Blinov, N.; Kozaczuk, J.; Morrissey, D.E.; de la Puente, A. Compressing the Inert Doublet Model. *Phys. Rev. D* **2016**, *93*, 035020, doi:10.1103/PhysRevD.93.035020.
20. Ilnicka, A.; Krawczyk, M.; Robens, T. Inert Doublet Model in light of LHC Run I and astrophysical data. *Phys. Rev.* **2016**, *D93*, 055026, doi:10.1103/PhysRevD.93.055026.
21. Hashemi, M.; Krawczyk, M.; Najjari, S.; Żarnecki, A.F. Production of Inert Scalars at the high energy e^+e^- colliders. *J. High Energy Phys.* **2016**, *02*, 187, doi:10.1007/JHEP02(2016)187.
22. Arhrib, A.; Benbrik, R.; El Falaki, J.; Jueid, A. Radiative corrections to the Triple Higgs Coupling in the Inert Higgs Doublet Model. *J. High Energy Phys.* **2015**, *12*, 007, doi:10.1007/JHEP12(2015)007.
23. Poulose, P.; Sahoo, S.; Sridhar, K. Exploring the Inert Doublet Model through the dijet plus missing transverse energy channel at the LHC. *Phys. Lett. B* **2017**, *765*, 300–306, doi:10.1016/j.physletb.2016.12.022.
24. Datta, A.; Ganguly, N.; Khan, N.; Rakshit, S. Exploring collider signatures of the inert Higgs doublet model. *Phys. Rev. D* **2017**, *95*, 015017, doi:10.1103/PhysRevD.95.015017.
25. Hashemi, M.; Najjari, S. Observability of Inert Scalars at the LHC. *Eur. Phys. J. C* **2017**, *77*, 592, doi:10.1140/epjc/s10052-017-5159-0.
26. Kanemura, S.; Kikuchi, M.; Sakurai, K. Testing the dark matter scenario in the inert doublet model by future precision measurements of the Higgs boson couplings. *Phys. Rev. D* **2016**, *94*, 115011, doi:10.1103/PhysRevD.94.115011.
27. Akeroyd, A.G.; others. Prospects for charged Higgs searches at the LHC. *Eur. Phys. J. C* **2017**, *77*, 276, doi:10.1140/epjc/s10052-017-4829-2.
28. Biondini, S.; Laine, M. Re-derived overclosure bound for the inert doublet model. *J. High Energy Phys.* **2017**, *08*, 047, doi:10.1007/JHEP08(2017)047.
29. Wan, N.; Li, N.; Zhang, B.; Yang, H.; Zhao, M.F.; Song, M.; Li, G.; Guo, J.Y. Searches for Dark Matter via Mono-W Production in Inert Doublet Model at the LHC. *Commun. Theor. Phys.* **2018**, *69*, 617, doi:10.1088/0253-6102/69/5/617.
30. Ilnicka, A.; Robens, T.; Stefaniak, T. Constraining Extended Scalar Sectors at the LHC and beyond. *Mod. Phys. Lett. A* **2018**, *33*, 1830007, doi:10.1142/S0217732318300070.
31. Belyaev, A.; Fernandez Perez Tomei, T.R.; Mercadante, P.G.; Moon, C.S.; Moretti, S.; Novaes, S.F.; Panizzi, L.; Rojas, F.; Thomas, M. Advancing LHC probes of dark matter from the inert two-Higgs-doublet model with the monojet signal. *Phys. Rev. D* **2019**, *99*, 015011, doi:10.1103/PhysRevD.99.015011.
32. Kalinowski, J.; Kotlarski, W.; Robens, T.; Sokolowska, D.; Zarnecki, A.F. Benchmarking the Inert Doublet Model for e^+e^- colliders. *J. High Energy Phys.* **2018**, *12*, 081, doi:10.1007/JHEP12(2018)081.
33. Kalinowski, J.; Kotlarski, W.; Robens, T.; Sokolowska, D.; Zarnecki, A.F. Exploring Inert Scalars at CLIC. *J. High Energy Phys.* **2019**, *07*, 053, doi:10.1007/JHEP07(2019)053.
34. Dercks, D.; Robens, T. Constraining the Inert Doublet Model using Vector Boson Fusion. *Eur. Phys. J. C* **2019**, *79*, 924, doi:10.1140/epjc/s10052-019-7436-6.
35. Bhardwaj, A.; Konar, P.; Mandal, T.; Sadhukhan, S. Probing the inert doublet model using jet substructure with a multivariate analysis. *Phys. Rev. D* **2019**, *100*, 055040, doi:10.1103/PhysRevD.100.055040.
36. Kanemura, S.; Kikuchi, M.; Mawatari, K.; Sakurai, K.; Yagyu, K. Full next-to-leading-order calculations of Higgs boson decay rates in models with non-minimal scalar sectors. *Nucl. Phys. B* **2019**, *949*, 114791, doi:10.1016/j.nuclphysb.2019.114791.
37. Banerjee, S.; Boudjema, F.; Chakrabarty, N.; Chalons, G.; Sun, H. Relic density of dark matter in the inert doublet model beyond leading order: The heavy mass case. *Phys. Rev. D* **2019**, *100*, 095024, doi:10.1103/PhysRevD.100.095024.
38. Tsai, Y.L.S.; Tran, V.Q.; Lu, C.T. Confronting dark matter co-annihilation of Inert two Higgs Doublet Model with a compressed mass spectrum. *J. High Energy Phys.* **2020**, *06*, 033, doi:10.1007/JHEP06(2020)033.
39. Braathen, J.; Kanemura, S. On two-loop corrections to the Higgs trilinear coupling in models with extended scalar sectors. *Phys. Lett. B* **2019**, *796*, 38–46, doi:10.1016/j.physletb.2019.07.021.
40. Braathen, J.; Kanemura, S. Leading two-loop corrections to the Higgs boson self-couplings in models with extended scalar sectors. *Eur. Phys. J. C* **2020**, *80*, 227, doi:10.1140/epjc/s10052-020-7723-2.
41. Guo-He, Y.; Mao, S.; Gang, L.; Yu, Z.; Jian-You, G. Searches for dark matter via charged Higgs pair production in the Inert Doublet Model at $\gamma\gamma$ collider. *arXiv* **2020**, arXiv:2006.06216.
42. Abouabid, H.; Arhrib, A.; Benbrik, R.; Falaki, J.E.; Gong, B.; Xie, W.; Yan, Q.S. One-loop radiative corrections to $e^+e^- \to Zh^0/H^0A^0$ in the Inert Higgs Doublet Model. *J. High Energy Phys.* **2021**, *05*, 100, doi:10.1007/JHEP05(2021)100.

43. Fabian, S.; Goertz, F.; Jiang, Y. Dark Matter and Nature of Electroweak Phase Transition with an Inert Doublet. *arXiv* **2020**, arXiv:2012.12847.
44. Basu, R.; Banerjee, S.; Pandey, M.; Majumdar, D. Lower bounds on dark matter annihilation cross-sections by studying the fluctuations of 21-cm line with dark matter candidate in inert doublet model (IDM) with the combined effects of dark matter scattering and annihilation. *arXiv* **2020**, arXiv:2010.11007.
45. Jangid, S.; Bandyopadhyay, P. Distinguishing Inert Higgs Doublet and Inert Triplet Scenarios. *Eur. Phys. J. C* **2020**, *80*, 715, doi:10.1140/epjc/s10052-020-8271-5.
46. Banerjee, S.; Boudjema, F.; Chakrabarty, N.; Sun, H. Relic density of dark matter in the inert doublet model beyond leading order for the low mass region: 1. Renormalisation and constraints. *arXiv* **2021**, arXiv:2101.02165.
47. Banerjee, S.; Boudjema, F.; Chakrabarty, N.; Sun, H. Relic density of dark matter in the inert doublet model beyond leading order for the low mass region: 2. Co-annihilation. *arXiv* **2021**, arXiv:2101.02166.
48. Banerjee, S.; Boudjema, F.; Chakrabarty, N.; Sun, H. Relic density of dark matter in the inert doublet model beyond leading order for the low mass region: 3. Annihilation in 3-body final state. *arXiv* **2021**, arXiv:2101.02167.
49. Banerjee, S.; Boudjema, F.; Chakrabarty, N.; Sun, H. Relic density of dark matter in the inert doublet model beyond leading order for the low mass region: 4. The Higgs resonance region. *arXiv* **2021**, arXiv:2101.02170.
50. Yang, F.X.; Han, Z.L.; Jin, Y. Same-Sign Dilepton Signature in the Inert Doublet Model. *Chin. Phys. C* **2021**, doi:10.1088/1674-1137/abf828.
51. De Blas, J.; Franceschini, R.; Riva, F.; Roloff, P.; Schnoor, U.; Spannowsky, M.; Wells, J.D.; Wulzer, A.; Zupan, J.; Alipour-Fard, S.; Altmannshofer, W.; et al. The CLIC Potential for New Physics. *arXiv* **2018**, arXiv:1812.02093., doi:10.23731/CYRM-2018-003
52. Alwall, J.; Herquet, M.; Maltoni, F.; Mattelaer, O.; Stelzer, T. MadGraph 5: Going Beyond. *J. High Energy Phys.* **2011**, *6*, 128, doi:10.1007/JHEP06(2011)128.
53. Available online: https://feynrules.irmp.ucl.ac.be/wiki/ModelDatabaseMainPage (accessed on 18 December 2020).
54. Zyla, P.A.; Barnett, R. M.; Beringer, J.; Dahl, O.; Dwyer, D. A.; Groom, D. E.; Lin, C. -J.; Lugovsky, K. S.; Pianori, E.; Robinson, D. J.; others. Review of Particle Physics. *Progress Theor. Exp. Phys.* **2020**, *2020*, 083C01, doi:10.1093/ptep/ptaa104.
55. Available online: https://twiki.cern.ch/twiki/bin/view/AtlasPublic/SupersymmetryPublicResults (accessed on 26 April 2021).
56. Available online: https://twiki.cern.ch/twiki/bin/view/CMSPublic/PhysicsResultsSUS (accessed on 26 April 2021).
57. Ipek, S.; McKeen, D.; Nelson, A.E. A Renormalizable Model for the Galactic Center Gamma Ray Excess from Dark Matter Annihilation. *Phys. Rev. D* **2014**, *90*, 055021, doi:10.1103/PhysRevD.90.055021.
58. No, J.M. Looking through the pseudoscalar portal into dark matter: Novel mono-Higgs and mono-Z signatures at the LHC. *Phys. Rev. D* **2016**, *93*, 031701, doi:10.1103/PhysRevD.93.031701.
59. Goncalves, D.; Machado, P.A.N.; No, J.M. Simplified Models for Dark Matter Face their Consistent Completions. *Phys. Rev. D* **2017**, *95*, 055027, doi:10.1103/PhysRevD.95.055027.
60. Bauer, M.; Haisch, U.; Kahlhoefer, F. Simplified dark matter models with two Higgs doublets: I. Pseudoscalar mediators. *J. High Energy Phys.* **2017**, *05*, 138, doi:10.1007/JHEP05(2017)138.
61. Tunney, P.; No, J.M.; Fairbairn, M. Probing the pseudoscalar portal to dark matter via $\bar{b}bZ(\to \ell\ell)+ \not{E}_T$: From the LHC to the Galactic Center excess. *Phys. Rev. D* **2017**, *96*, 095020, doi:10.1103/PhysRevD.96.095020.
62. Abe, T.; Afik, Y.; Albert, A.; Anelli, C.R.; Barak, L.; Bauer, M.; Behr, J.K.; Bell, N.F.; Boveia, A.; Brandt, O.; Busoni, G.; et al. LHC Dark Matter Working Group: Next-generation spin-0 dark matter models. *Phys. Dark Univ.* **2020**, *27*, 100351, doi:10.1016/j.dark.2019.100351.
63. Robens, T. The THDMa revisited—A preview. *arXiv* **2021**, arXiv:2105.06231.
64. Ginzburg, I.F.; Kanishev, K.A.; Krawczyk, M.; Sokolowska, D. Evolution of Universe to the present inert phase. *Phys. Rev. D* **2010**, *82*, 123533, doi:10.1103/PhysRevD.82.123533.
65. The ATLAS Collaboration. Measurement of the Higgs boson mass in the $H \to ZZ^* \to 4\ell$ and $H \to \gamma\gamma$ channels with $\sqrt{s} = 13$ TeV pp collisions using the ATLAS detector. *Phys. Lett. B* **2018**, *784*, 345–366, doi:10.1016/j.physletb.2018.07.050.
66. Mondal, K. Measurements of Higgs Boson Production and Properties in Di-photon Decay Channel Using Data Collected by CMS Detector at Center of Mass Energy of 13 TeV. *Springer Proc. Phys.* **2018**, *203*, 201–204, doi:10.1007/978-3-319-73171-1_45.
67. Sirunyan, A.M.; Tumasyan, A.; Adam, W.; Ambrogi, F.; Asilar, E.; Bergauer, T.; Brandstetter, J.; Dragicevic, M.; Erö, J.; Escalante Del Valle, A.; et al. Measurements of the Higgs boson width and anomalous HVV couplings from on-shell and off-shell production in the four-lepton final state. *Phys. Rev. D* **2019**, *99*, 112003, doi:10.1103/PhysRevD.99.112003.
68. The ATLAS Collaboration. *Combination of Searches for Invisible Higgs Boson Decays with the ATLAS Experiment*; Technical Report ATLAS-CONF-2020-052; CERN: Geneva, Switzerland, 2020.
69. Bechtle, P.; Heinemeyer, S.; Stal, O.; Stefaniak, T.; Weiglein, G. *HiggsSignals*: Confronting arbitrary Higgs sectors with measurements at the Tevatron and the LHC. *Eur. Phys. J. C* **2014**, *74*, 2711, doi:10.1140/epjc/s10052-013-2711-4.
70. Bechtle, P.; Heinemeyer, S.; Klingl, T.; Stefaniak, T.; Weiglein, G.; Wittbrodt, J. HiggsSignals-2: Probing new physics with precision Higgs measurements in the LHC 13 TeV era. *Eur. Phys. J. C* **2021**, *81*, 145, doi:10.1140/epjc/s10052-021-08942-y.
71. Altarelli, G.; Barbieri, R. Vacuum polarization effects of new physics on electroweak processes. *Phys. Lett. B* **1991**, *253*, 161–167, doi:10.1016/0370-2693(91)91378-9.
72. Peskin, M.E.; Takeuchi, T. A New constraint on a strongly interacting Higgs sector. *Phys. Rev. Lett.* **1990**, *65*, 964–967, doi:10.1103/PhysRevLett.65.964.

73. Peskin, M.E.; Takeuchi, T. Estimation of oblique electroweak corrections. *Phys. Rev. D* **1992**, *46*, 381–409, doi:10.1103/PhysRevD.46.381.
74. Maksymyk, I.; Burgess, C.P.; London, D. Beyond S, T and U. *Phys. Rev. D* **1994**, *50*, 529–535, doi:10.1103/PhysRevD.50.529.
75. Available online: http://project-gfitter.web.cern.ch/project-gfitter/ (accessed on 26 April 2021).
76. Haller, J.; Hoecker, A.; Kogler, R.; Moenig, K.; Peiffer, T.; Stelzer, J. Update of the global electroweak fit and constraints on two-Higgs-doublet models. *Eur. Phys. J. C* **2018**, *78*, 675, doi:10.1140/epjc/s10052-018-6131-3.
77. Eriksson, D.; Rathsman, J.; Stål, O. 2HDMC: Two-Higgs-Doublet Model Calculator Physics and Manual. *Comput. Phys. Commun.* **2010**, *181*, 189–205, doi:10.1016/j.cpc.2009.09.011.
78. Pierce, A.; Thaler, J. Natural Dark Matter from an Unnatural Higgs Boson and New Colored Particles at the TeV Scale. *J. High Energy Phys.* **2007**, *08*, 026, doi:10.1088/1126-6708/2007/08/026.
79. Heisig, J.; Kraml, S.; Lessa, A. Constraining new physics with searches for long-lived particles: Implementation into SModelS. *Phys. Lett. B* **2019**, *788*, 87–95, doi:10.1016/j.physletb.2018.10.049.
80. Belyaev, A.; Prestel, S.; Rojas-Abbate, F.; Zurita, J. Probing Dark Matter with Disappearing Tracks at the LHC. *Phys. Rev. D* **2021**, *103*, 095006, doi:10.1103/PhysRevD.103.095006.
81. Bechtle, P.; Brein, O.; Heinemeyer, S.; Weiglein, G.; Williams, K.E. HiggsBounds: Confronting Arbitrary Higgs Sectors with Exclusion Bounds from LEP and the Tevatron. *Comput. Phys. Commun.* **2010**, *181*, 138–167, doi:10.1016/j.cpc.2009.09.003.
82. Bechtle, P.; Brein, O.; Heinemeyer, S.; Weiglein, G.; Williams, K.E. HiggsBounds 2.0.0: Confronting Neutral and Charged Higgs Sector Predictions with Exclusion Bounds from LEP and the Tevatron. *Comput. Phys. Commun.* **2011**, *182*, 2605–2631, doi:10.1016/j.cpc.2011.07.015.
83. Bechtle, P.; Brein, O.; Heinemeyer, S.; Stål, O.; Stefaniak, T.; Weiglein, G.; Williams, K.E. HiggsBounds − 4: Improved Tests of Extended Higgs Sectors against Exclusion Bounds from LEP, the Tevatron and the LHC. *Eur. Phys. J. C* **2014**, *74*, 2693, doi:10.1140/epjc/s10052-013-2693-2.
84. Bechtle, P.; Heinemeyer, S.; Stål, O.; Stefaniak, T.; Weiglein, G. Applying Exclusion Likelihoods from LHC Searches to Extended Higgs Sectors. *Eur. Phys. J. C* **2015**, *75*, 421, doi:10.1140/epjc/s10052-015-3650-z.
85. Bechtle, P.; Dercks, D.; Heinemeyer, S.; Klingl, T.; Stefaniak, T.; Weiglein, G.; Wittbrodt, J. HiggsBounds-5: Testing Higgs Sectors in the LHC 13 TeV Era. *Eur. Phys. J. C* **2020**, *80*, 1211, doi:10.1140/epjc/s10052-020-08557-9.
86. Aghanim, N.; Akrami, Y.; Ashdown, M.; Aumont, J.; Baccigalupi, C.; Ballardini, M.; Banday, A.J.; Barreiro, R.B.; Bartolo, N.; Basak, S.; et al. Planck 2018 results. VI. Cosmological parameters. *Astron. Astrophys.* **2020**, *641*, A6, doi:10.1051/0004-6361/201833910.
87. Aprile, E., et al.; XENON Collaboration. Dark Matter Search Results from a One Tonne×Year Exposure of XENON1T. *Phys. Rev. Lett.* **2018**, *121*, 111302, doi:10.1103/PhysRevLett.121.111302.
88. Belyaev, A.; Blandford, J.; Locke, D. PhenoData Database. January 2017. Available online: https://hepmdb.soton.ac.uk/phenodata (accessed on 26 April 2021).
89. Belanger, G.; Boudjema, F.; Goudelis, A.; Pukhov, A.; Zaldivar, B. micrOMEGAs5.0 : Freeze-in. *Comput. Phys. Commun.* **2018**, *231*, 173–186, doi:10.1016/j.cpc.2018.04.027.
90. Belanger, G.; Mjallal, A.; Pukhov, A. Recasting direct detection limits within micrOMEGAs and implication for non-standard Dark Matter scenarios. *Eur. Phys. J. C* **2021**, *81*, 239, doi:10.1140/epjc/s10052-021-09012-z.
91. Belyaev, A.; Cacciapaglia, G.; Ivanov, I.P.; Rojas-Abatte, F.; Thomas, M. Anatomy of the Inert Two Higgs Doublet Model in the light of the LHC and non-LHC Dark Matter Searches. *Phys. Rev. D* **2018**, *97*, 035011, doi:10.1103/PhysRevD.97.035011.
92. Lopez Honorez, L.; Yaguna, C.E. A new viable region of the inert doublet model. *J. Cosmol. Astropart. Phys.* **2011**, *1101*, 002, doi:10.1088/1475-7516/2011/01/002.
93. Hambye, T.; Ling, F.S.; Lopez Honorez, L.; Rocher, J. Scalar Multiplet Dark Matter. *J. High Energy Phys.* **2009**, *7*, 090.
94. Twiki for HL/HE-LHC Physics Workshop. Available online: https://twiki.cern.ch/twiki/bin/view/LHCPhysics/HLHELHCWorkshop (accessed on 26 April 2021).
95. Abada, A.; Abbrescia, M.; AbdusSalam, S.S.; Abdyukhanov, I.; Abelleira Fernandez, J.; Abramov, A.; Aburaia, M.; Acar, A.O.; Adzic, P.R.; Agrawal, P.; et al. HE-LHC: The High-Energy Large Hadron Collider. *Eur. Phys. J. Spec. Top.* **2019**, *228*, 1109–1382, doi:10.1140/epjst/e2019-900088-6.
96. Abada, A.; Abbrescia, M.; AbdusSalam, S.S.; Abdyukhanov, I.; Abelleria Fernandez, J.A.; Abramov, A.; Aburaia, M.; Acar, A.O.; Adzic, P.R.; Agrawal, P.; et al. FCC-hh: The Hadron Collider. *Eur. Phys. J. Spec. Top.* **2019**, *228*, 755–1107, doi:10.1140/epjst/e2019-900087-0.
97. Ellis, R.K.; Heinemann, B.; de Blas, J.; Cepeda, M.; Grojean, C.; Maltoni, F.; Nisati, A.; Petit, E.; Rattazzi, R.; Verkerke, W.; et al. Physics Briefing Book : Input for the European Strategy for Particle Physics Update 2020; *arXiv* **2019**, arXiv:1910.11775
98. Adamczyk, L.; Banaś, E.; Brandt, A.; Bruschi, M.; Grinstein, S.; Lange, J.; Rijssenbeek, M.; Sicho, P.; Staszewski, R.; Sykora, T.; et al. *Technical Design Report for the ATLAS Forward Proton Detector*; Technical Report, CERN-LHCC-2015-009, ATLAS-TDR-024; CERN: Geneva, Switzerland, 2015.
99. Albrow, M.; Arneodo, M.; Avati, V.; Baechler, J.; Cartiglia, N.; Deile, M.; Gallinaro, M.; Hollar, J.; Lo Vetere, M.; Oesterberg, K.; et al. *CMS-TOTEM Precision Proton Spectrometer*; Technical Report, CERN-LHCC-2014-021, TOTEM-TDR-003, CMS-TDR-13; CERN: Geneva, Switzerland, 2014.
100. CMS Collaboration. The CMS Precision Proton Spectrometer at the HL-LHC—Expression of Interest. *arXiv* **2021**, arXiv:2103.02752.

101. First Collaboration Meeting on Physics and Experiments at a Muon Collider. Available online: https://indico.cern.ch/event/939986/ (accessed on 26 April 2021).
102. Chakrabarty, N.; Han, T.; Liu, Z.; Mukhopadhyaya, B. Radiative Return for Heavy Higgs Boson at a Muon Collider. *Phys. Rev. D* **2015**, *91*, 015008, doi:10.1103/PhysRevD.91.015008.
103. Delahaye, J.P.; Diemoz, M.; Long, K.; Mansoulié, B.; Pastrone, N.; Rivkin, L.; Schulte, D.; Skrinsky, A.; Wulzer, A. Muon Colliders. *arXiv* **2019**, arXiv:1901.06150.
104. Zarnecki, A.F.; Kalinowski, J.; Klamka, J.; Sopicki, P.; Kotlarski, W.; Robens, T.; Sokolowska, D. Searching Inert Scalars at Future e^+e^- Colliders. In Proceedings of the International Workshop on Future Linear Colliders (LCWS 2019) Sendai, Miyagi, Japan, 28 October–1 November 2019.
105. Zarnecki, A.F.; Kalinowski, J.; Klamka, J.; Sopicki, P.; Kotlarski, W.; Robens, T.N.; Sokolowska, D. Searching inert scalars at future e^+e^- colliders. *PoS* **2020**, *CORFU2019*, 047, doi:10.22323/1.376.0047.
106. Klamka, J.F. Searching for Inert Doublet Model scalars at high energy CLIC. Ph.D. Thesis, Faculty of Physics, University of Warsaw, Warsaw, Poland, 1 July 2020.